

# Measurement of direct photon production at Tevatron fixed target energies

L. Apanasevich,<sup>1,2</sup> J. Bacigalupi,<sup>3</sup> W. Baker,<sup>4</sup> M. Begel,<sup>2</sup> S. Blusk,<sup>5</sup> C. Bromberg,<sup>1</sup> P. Chang,<sup>6</sup> B. Choudhary,<sup>7</sup> W. H. Chung,<sup>5</sup> L. de Barbaro,<sup>2</sup> W. DeSoi,<sup>2</sup> W. Długosz,<sup>6</sup> J. Dunlea,<sup>2</sup> E. Engels, Jr.,<sup>5</sup> G. Fanourakis,<sup>2</sup> T. Ferbel,<sup>2</sup> J. Ftacnik,<sup>2</sup> D. Garelick,<sup>6</sup> G. Ginther,<sup>2</sup> M. Glaubman,<sup>6</sup> P. Gutierrez,<sup>8</sup> K. Hartman,<sup>9</sup> J. Huston,<sup>1</sup> C. Johnstone,<sup>4</sup> V. Kapoor,<sup>7</sup> J. Kuehler,<sup>8</sup> C. Lirakis,<sup>6</sup> F. Lobkowicz,<sup>2,\*</sup> P. Lukens,<sup>4</sup> J. Mansour,<sup>2</sup> A. Maul,<sup>1</sup> R. Miller,<sup>1</sup> B. Y. Oh,<sup>9</sup> G. Osborne,<sup>2</sup> D. Pellett,<sup>3</sup> E. Prebys,<sup>2</sup> R. Roser,<sup>2</sup> P. Shepard,<sup>5</sup> R. Shivpuri,<sup>7</sup> D. Skow,<sup>4</sup> P. Slattery,<sup>2</sup> L. Sorrell,<sup>1</sup> D. Striley,<sup>6</sup> W. Toothacker,<sup>9,\*</sup> S. M. Tripathi,<sup>3</sup> N. Varelas,<sup>2</sup> D. Weerasundara,<sup>5</sup> J. J. Whitmore,<sup>9</sup> T. Yasuda,<sup>6</sup> C. Yosef,<sup>1</sup> M. Zieliński,<sup>2</sup> and V. Zutshi<sup>7</sup>

(Fermilab E706 Collaboration)

<sup>1</sup>Michigan State University, East Lansing, Michigan 48824

<sup>2</sup>University of Rochester, Rochester, New York 14627

<sup>3</sup>University of California-Davis, Davis, California 95616

<sup>4</sup>Fermi National Accelerator Laboratory, Batavia, Illinois 60510

<sup>5</sup>University of Pittsburgh, Pittsburgh, Pennsylvania 15260

<sup>6</sup>Northeastern University, Boston, Massachusetts 02115

<sup>7</sup>University of Delhi, Delhi, India 110007

<sup>8</sup>University of Oklahoma, Norman, Oklahoma 73019

<sup>9</sup>Pennsylvania State University, University Park, Pennsylvania 16802

(Dated: November 10, 2018)

Measurements of the production of high transverse momentum direct photons by a 515 GeV/c  $\pi^-$  beam and 530 and 800 GeV/c proton beams in interactions with beryllium and hydrogen targets are presented. The data span the kinematic ranges of  $3.5 < p_T < 12$  GeV/c in transverse momentum and 1.5 units in rapidity. The inclusive direct-photon cross sections are compared with next-to-leading-order perturbative QCD calculations and expectations based on a phenomenological parton- $k_T$  model.

PACS numbers: 13.85.Qk, 12.38.Qk

## I. INTRODUCTION

Inclusive single-particle production at large transverse momentum ( $p_T$ ) has been useful in the development of perturbative quantum chromodynamics (PQCD) [1–4]. Quantitative comparisons with data have yielded information on the validity of the PQCD description, and on parton distribution functions of hadrons (PDF) and the fragmentation functions of partons. This paper reports precision measurements of the production of direct photons with large  $p_T$ .

At leading order, only two processes contribute to the direct-photon cross section, namely,  $q\bar{q}$  annihilation and

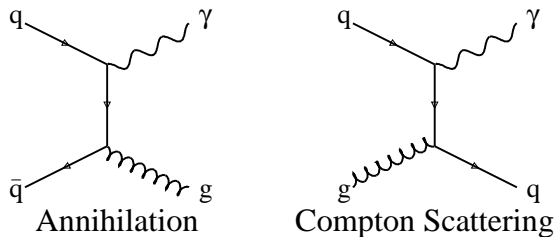


FIG. 1: Leading-order diagrams for direct-photon production.

quark–gluon Compton scattering (Fig. 1). The photon’s momentum reflects the collision kinematics since such photons are produced at the elementary interaction vertex. This contrasts with jet production, where the hadronization process obscures the measurement of energy and direction of the outgoing parton. A complete theoretical description of the direct-photon process is of special importance as it has long been expected to facilitate the extraction of the gluon distribution of the proton. The quark–gluon Compton scattering process shown in Fig. 1 provides a major contribution to inclusive direct-photon production. The gluon distribution is relatively well constrained by deep-inelastic and Drell-Yan data for momentum fractions  $x < 0.1$ , but less so at larger  $x$  [5]. Fixed-target direct-photon data were incorporated into several previous global parton-distribution analyses [6–8] to constrain the gluon distribution at large  $x$ , but more recent global PDF analyses have not included such photon data; this point is revisited in the concluding section of this work.

## II. APPARATUS

### A. Meson West spectrometer

Fermilab E706 is a fixed-target experiment designed to measure the production of direct photons, neutral

\*Deceased

mesons, and associated particles at high- $p_T$  [9–13]. The apparatus included a charged particle spectrometer, a large liquid argon calorimeter and downstream muon identifiers.

The data collection phase of this experiment spanned three fixed-target running periods, including the relatively low-statistics commissioning run during 1987–1988 [14, 15], and the two primary data runs in 1990 and 1991–1992. This paper reports on data from the two primary data runs of the experiment [16]. During the 1990 run, the target consisted of two 0.8 mm thick copper foils followed by two pieces of beryllium. The upstream piece was 3.7 cm long, while the length of the downstream piece was 1.1 cm. In the 1991–1992 run, the target consisted of two 0.8 mm thick copper foils immediately upstream of a liquid hydrogen target [17], followed by a 2.54 cm long beryllium cylinder. The liquid hydrogen was contained in a 15.3 cm long mylar flask, which was supported in an evacuated volume with beryllium windows at each end (2.5 mm thickness upstream and 2.8 mm thickness downstream).

The charged particle spectrometer consisted of silicon microstrip detectors (SSDs) in the target region and multiwire proportional chambers (PWCs) and straw tube drift chambers (STDCs) downstream of a large-aperture analysis magnet [12]. Six  $3 \times 3$  cm<sup>2</sup> SSD planes were located upstream of the target region and used to reconstruct beam tracks. Two hybrid  $5 \times 5$  cm<sup>2</sup> SSD planes (25  $\mu$ m pitch strips in the central 1 cm, 50  $\mu$ m beyond) were located downstream of the target region. These were followed by eight  $5 \times 5$  cm<sup>2</sup> SSD planes of 50  $\mu$ m pitch. The analysis dipole imparted a 0.45 GeV/ $c$   $p_T$  impulse in the horizontal plane to charged particles. Downstream track segments were measured by means of four stations of four views ( $XYUV$ ) of 2.54 mm pitch PWCs and two stations of eight ( $4X4Y$ ) layers of STDCs with tube diameters 1.03 cm (upstream station) and 1.59 cm (downstream station) [18].

Photons were detected in a large, lead and liquid-argon sampling electromagnetic calorimeter (EMLAC), located 9 m downstream of the target [19]. The EMLAC had a cylindrical geometry with an inner radius of 20 cm and an outer radius of 160 cm. The calorimeter had 33 longitudinal cells read out in two sections: an 11 cell front section (8.5 radiation lengths) and a 22 cell back section (18 radiation lengths). Each longitudinal cell consisted of a 2 mm thick lead cathode (the first cathode was constructed of aluminum), a double-sided copper-clad G-10 radial ( $R$ ) anode board, a second 2 mm thick lead cathode, and a double-sided copper-clad G-10 azimuthal ( $\Phi$ ) anode board. The 2.5 mm gaps between these layers were filled with liquid argon. The physical layout is illustrated in Fig. 2.

The EMLAC readout was subdivided azimuthally into octants, each consisting of interleaved, finely segmented, radial and azimuthal views. This segmentation was realized by cutting the copper-cladding on the anode boards to form either radial or azimuthal strips. Signals from

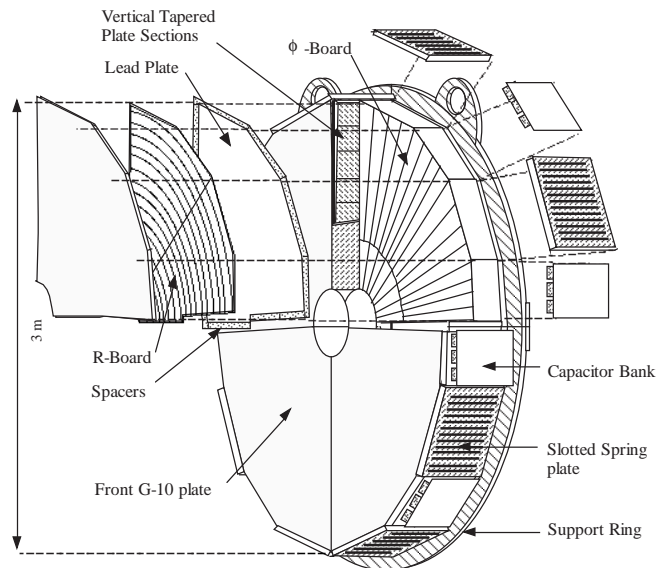


FIG. 2: A drawing of the liquid argon electromagnetic calorimeter with some components pulled away in one quadrant to reveal a view of the internal details.

corresponding strips from all  $R$  (or  $\Phi$ ) anode boards in the front (or back) section of a given octant were jumpered together. The copper-cladding on the radial anode boards was cut into concentric strips centered on the nominal beam axis. The width of the strips on the first  $R$  board was 5.5 mm. The width of the strips on the following  $R$  boards increased slightly so that the radial geometry was projective relative to the target region. The azimuthal strips were split at a radius of 40 cm into inner and outer segments; each inner strip subtended an azimuthal angle of  $\pi/192$  radians, while outer strips covered  $\pi/384$  radians.

The spectrometer also included two other calorimeters: a hadronic calorimeter located downstream of the EMLAC within the same cryostat, and a steel and scintillator calorimeter positioned further downstream to increase coverage in the very forward region. The E672 muon spectrometer, consisting of a toroidal magnet, shielding, scintillator, and proportional wire chambers, was deployed immediately downstream of the calorimeters [20–23].

The spectrometer was located at the end of the Meson West beamline. The design of the beamline, primary target and primary beam dump were intended to minimize the rate of beam-halo muons incident upon the spectrometer. The beamline was capable of transporting either a primary (800 GeV/ $c$ ) proton beam or unseparated secondary particle beams of either polarity to the experimental hall. The beamline Čerenkov detector was used to identify the secondary beam particles [24]. This 43.4 m long helium-filled counter was located 100 m upstream of the experimental target. The positive secondary beam with mean momentum of 530 GeV/ $c$  was

97% protons. The negative secondary beam with mean momentum of 515 GeV/ $c$  was 99% pions.

At the end of the beamline was a 4.7 m long stack of steel surrounding the beam pipe and shadowing the EMLAC to absorb off-axis hadrons. A water tank was placed at the downstream end of this hadron shield to absorb low-energy neutrons. Surrounding the hadron shield and neutron absorber were walls of scintillation counters (VW) to identify penetrating muons. There was one wall at the upstream end and two walls at the downstream end of the hadron absorber during the 1990 run. An additional wall was added to the upstream end of the hadron absorber prior to the 1991-1992 run.

### B. Trigger

The E706 trigger selected interactions yielding high- $p_T$  showers in the EMLAC. The selection process involved several stages: beam and interaction definitions, a pre-trigger, and high- $p_T$  trigger requirements [10, 12, 25]. A scintillator hodoscope, located 2 m upstream of the target region, was used to detect beam particles, and reject interactions with more than one incident beam particle. Additional scintillator with a 1 cm diameter central hole was located just downstream of the beam hodoscope, and served to reject interactions initiated by particles in the beam halo [26]. Two pairs of scintillator counters, mounted on the dipole analysis magnet, were used to identify interactions in the target. A filter was employed for the high- $p_T$  triggers to reject interactions that occurred within 60 ns of one another to minimize potential confusion in the EMLAC due to out-of-time interactions.

For those interactions that satisfied the beam and interaction requirements, the  $p_T$  deposited in various regions of the EMLAC was evaluated by weighting the energy signals from the EMLAC  $R$ -channel amplifier fast outputs by a factor proportional to  $\sin\theta_i$ , where  $\theta_i$  was the polar angle between the  $i^{th}$  strip and the nominal beam axis. The PRETRIGGER HI requirement for a given octant was satisfied when the  $p_T$  detected in either the inner 128  $R$  channels or the outer  $R$  channels of that octant was greater than a threshold value. A pretrigger signal was issued only when there was no evidence in that octant of substantial noise, significant  $p_T$  attributable to an earlier interaction, or incident beam-halo muon detected by the VW.

Localized trigger groups were formed for each octant by clustering the  $R$ -channel fast-outputs into 32 groups of 8 channels. Each adjacent pair of 8 channel groups formed a group-of-16 strips. If the  $p_T$  detected in any of these groups-of-16 was above a specified high (or low) threshold, then a LOCAL HI (or LOCAL LO) signal was generated for that octant. A SINGLE LOCAL HI (or SINGLE LOCAL LO) trigger was generated if a LOCAL HI (or LOCAL LO) signal was generated in coincidence with the PRETRIGGER HI in the same octant.

Trigger decisions were also made based upon global

energy depositions within an octant. A GLOBAL LO signal was generated if the total  $p_T$  in an octant exceeded a threshold value. The LOCAL $\otimes$ GLOBAL LO trigger required a coincidence of the PRETRIGGER HI signal with GLOBAL LO and LOCAL LO signals from the same octant. The LOCAL LO requirement was included to suppress spurious global triggers due to coherent noise in the EMLAC.

The SINGLE LOCAL LO and LOCAL $\otimes$ GLOBAL LO triggers were prescaled to keep them from dominating the data sample. Prescaled samples of beam, interaction, and pretrigger events were also recorded.

## III. ANALYSIS METHODS

Data samples contributing to this analysis represent an integrated luminosity of 6.8 (1.1) pb $^{-1}$  for 530 GeV/ $c$   $p$ Be ( $pp$ ) interactions, and 6.5 (1.1) pb $^{-1}$  at 800 GeV/ $c$ . These samples were accumulated during the 1991-1992 run. Results reported in this paper also use 6.1 pb $^{-1}$  of  $\pi^-$ Be data recorded during the 1990 run, as well as 1.4 pb $^{-1}$  of  $\pi^-$ Be data and 0.23 pb $^{-1}$  of  $\pi^-p$  data accumulated during the 1991-1992 run. The following subsections describe the analysis procedures and methods used to correct the data for losses due to inefficiencies and selection biases. Additional details can be found in several of our previous papers [10–12, 19].

### A. Event reconstruction

Two major aspects of the analysis procedure involved charged-particle and calorimeter shower reconstruction. The charged-track reconstruction algorithm produced track segments upstream of the magnet using information from the SSDs, and downstream of the magnet using information from the PWCs and STDCs. These track segments were projected to the center of the magnet and linked to form the final tracks whose calculated charges and momenta were used for the physics analysis. The charged track reconstruction is described in more detail elsewhere [12].

The readout in each EMLAC quadrant consisted of four regions: left and right  $R$ , and inner and outer  $\Phi$ . Strip energies from clusters in each region were fit to the shape of an electromagnetic shower determined from detailed Monte Carlo simulations and isolated-shower data. These fits were used to evaluate the positions and energies of the peaks in each region. Shower positions and energies were obtained by correlating peaks of approximately the same energy in the  $R$  and  $\Phi$  regions within the same half octant. More complex algorithms were used to handle configurations with showers spanning multiple regions. The EMLAC readout was also subdivided longitudinally into front and back sections. This segmentation provided discrimination between showers generated by electromagnetically or hadronically interacting particles.

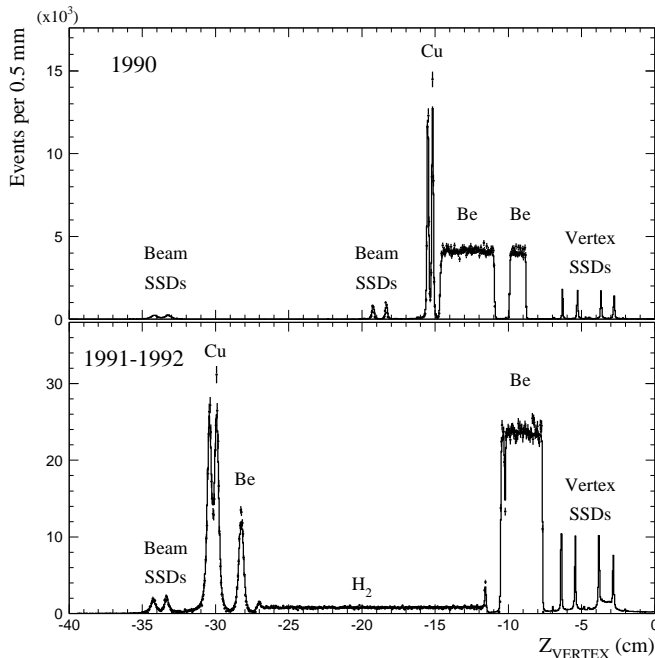


FIG. 3: The longitudinal distribution of reconstructed vertices for 1990 (top) and 1991-1992 (bottom) target configurations. The data are represented by the histogram, the results from the detailed detector simulation by the points.

An expanded discussion of the EMLAC reconstruction procedures and performance can be found elsewhere [19].

### B. Selection criteria and corrections

Only events with reconstructed vertices within the fiducial volume of the Be or  $H_2$  targets contribute to the results presented in this paper. Vertex reconstruction efficiencies were evaluated for each target using a detailed Monte Carlo simulation of the spectrometer, as described in Section III.F below [27]. These efficiencies were used to correct for reconstruction losses and resolution smearing across fiducial boundaries of the targets. The corrections were  $< 1\%$  for interactions in the beryllium targets in the 1990 configuration as well as for the hydrogen and downstream beryllium targets in the 1991-1992 configuration. The correction was  $< 3.5\%$  for the upstream Be target in the 1991-1992 configuration. The longitudinal distribution of reconstructed vertices are shown, for both 1990 and 1991-1992 target configurations, in Fig. 3. Overlaid on the data for the copper, beryllium, and hydrogen targets are the results from the detailed Monte Carlo simulation.

Only photons that were reconstructed with the fiducial regions of the EMLAC contributed to the cross-section results presented. In particular, regions of the detector near quadrant boundaries that abutted steel support plates, the central beam hole, the outer radius of the EMLAC, and octant boundaries were excluded. A sim-

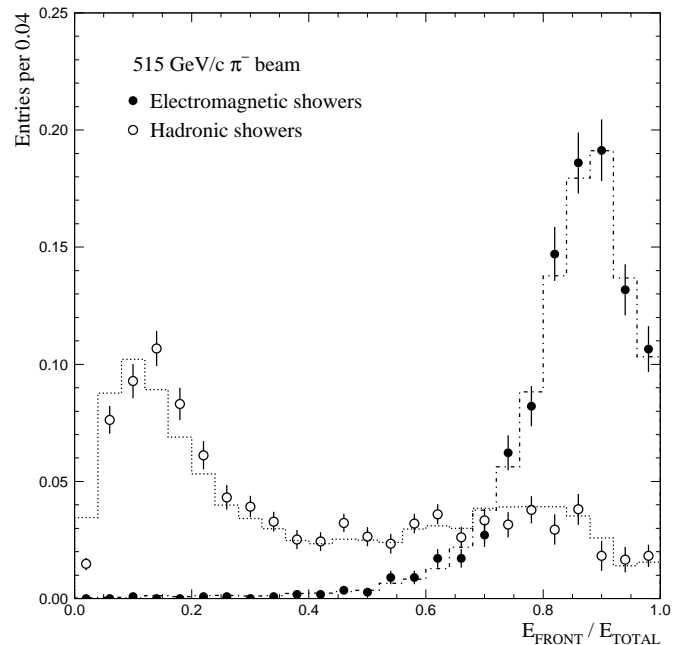


FIG. 4: Fraction of energy deposited in the front section of the EMLAC for identified electromagnetic showers (electrons from photon conversions) and hadronic showers (charged pions from  $K_s$  decays). The data are represented by the histograms, the results from the detailed detector simulation by the points. The distributions have been normalized to unit area.

ple ray-tracing Monte Carlo program was employed to determine the correction for the  $\Phi$ -dependent fiducial requirements.

Showers that deposited  $\leq 20\%$  of their energy in the front section of the EMLAC were not considered as photon candidates since such showers were likely to be due to hadronic interactions [19] (Fig. 4). Losses of photons due to this requirement were  $\approx 2\%$ . A detailed event simulation (described in Section III.F below) was employed to correct for this and other effects including reconstruction smearing and losses.

Reconstructed showers were excluded from the photon sample when charged-particle tracks pointed to within 1 cm of shower center (Fig. 5). The correction for this criterion in the direct-photon analysis is  $\approx 1.01$  based upon studies of the impact of this requirement on reconstructed  $\pi^0$ 's.

The correction for losses due to the conversion of photons into  $e^+e^-$  pairs was evaluated by projecting each reconstructed photon from the event vertex to the reconstructed position in the EMLAC. The radiation length of material traversed, up to the analysis magnet, was evaluated based upon detailed detector descriptions. The photon conversion probability was evaluated and used to account for conversion losses. The average correction for conversion losses was 1.09 per photon for the Be target in the 1990 run (1.08 in 1991-1992 run) and 1.11 per photon for the  $H_2$  target.

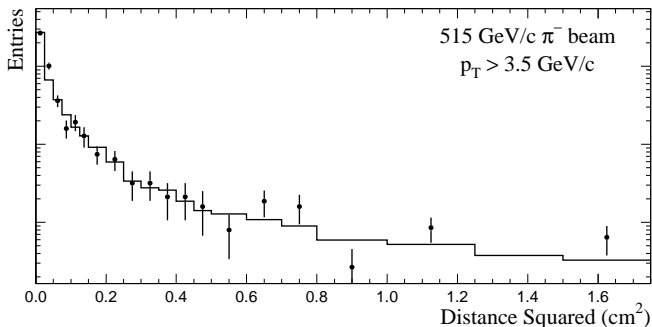


FIG. 5: Distribution of the distance squared between the reconstructed positions of electromagnetic showers and the nearest charged-particle track in data (histogram) and in the detailed detector simulation ( $\bullet$ ). To enhance the electron fraction in these samples, only showers with  $> 0.75$  of their energy deposited in the front section of the EMLAC contribute to this plot. The distributions have been normalized to the same area.

### C. Trigger corrections

Trigger corrections were evaluated on an event-by-event basis using the energy depositions detected in the EMLAC combined with the measured responses of the trigger groups in which those energy depositions occurred for this particular trigger and event. The probability ( $p_i$ ) that the  $i^{\text{th}}$  trigger group (e.g., a group-of-16 or inner 128  $R$  channels) in the octant was satisfied was measured as a function of the  $p_T$  reconstructed within the group using data samples unbiased with respect to that group [25]. The trigger probability for a given octant was defined as  $P = 1 - \prod(1 - p_i)$ . Trigger corrections were evaluated on an event-by-event basis by applying the inverse of the trigger probability as a weight to each photon candidate. Photon candidates with  $P < 0.1$  were excluded from further consideration to avoid excessively large weights. The correction for losses from this requirement was determined from the detailed detector simulation and absorbed into the reconstruction efficiency described below.

The results presented in this paper are extracted from data selected using several triggers with different thresholds and prescale factors to probe a broad range of  $p_T$ . The lower threshold and prescaled triggers are used to populate the lower  $p_T$  range where the data from the higher threshold triggers were judged to be less reliable (due to larger average trigger corrections) than corresponding data from the lower threshold triggers. These judgements were made by comparing the fully corrected results from each trigger in  $p_T$  and rapidity,  $y_{\text{cm}}$ . These transitions were functions of both  $p_T$  and  $y_{\text{cm}}$ , and were different for the three samples. The SINGLE LOCAL HI trigger was used exclusively for photons with  $p_T > 4.0$  GeV/ $c$ .

### D. Rejection of beam-halo muons

Spurious triggers were produced by muons in the beam halo that deposited significant energy in the EMLAC in random coincidence with interactions in the target. Such muon-induced showers were interpreted by the trigger as high- $p_T$  depositions, particularly when they occurred in the outer regions of the EMLAC. While the pretrigger logic used VW signals to reject events associated with such muons, additional requirements on the latched VW signals, the total  $p_T$  imbalance in the event, and the direction and shape of reconstructed showers were imposed during the offline analysis to further suppress this background. We note that these criteria successfully eliminated the beam-halo muon background in the high- $p_T$  meson samples (see Fig. 6 of Ref. [10] and Fig. 5 of Ref. [11]). As expected, the beam-halo muons rates were much larger in the secondary beam data samples than in the primary beam (800 GeV/ $c$ ) data sample.

The  $p_T$  balance in the event was defined by calculating the  $p_T$  of the photons and charged particles which, based upon their initial trajectories, would intercept the EMLAC in the transverse plane within the  $120^\circ$  sector opposite the direct-photon candidate. The ratio of this “away-side”  $p_T$  ( $P_T^{\text{away}}$ ) to that of the direct-photon candidate should be near unity in interactions that generate a high- $p_T$  photon. However, for events triggered by showers from beam-halo muons,  $P_T^{\text{away}}/p_T$  should be near zero, since interactions are typically soft. Showers with  $P_T^{\text{away}}/p_T < 0.3$  were excluded from the photon sample.

A measure of the incident direction of showers observed in the EMLAC was characterized as  $\delta = R_{\text{front}} - (Z_{\text{front}}/Z_{\text{back}})R_{\text{back}}$ , where  $R_{\text{front}}$  and  $R_{\text{back}}$  are the radial positions of the reconstructed shower in the front and back sections, and  $Z_{\text{front}}$  and  $Z_{\text{back}}$  are the longitudinal locations of those EMLAC sections relative to the nominal target location. Showers with  $\delta \sim 0$  were generated by particles from the target region, while showers with large  $\delta$  were generated by particles incident from other directions. The requirement on  $\delta$  was a function of radius; showers with  $\delta > 0.193$  cm for  $R < 40$  cm ( $\delta > 0.0048R$  for  $R \geq 40$  cm) were excluded from the photon sample.

The electromagnetic shower shape employed in the photon reconstruction program was determined for photons originating in the target region [19]. Consequently, showers resulting from beam-halo muons were frequently poorly fit by this shower shape, particularly in the radial view. The  $\chi^2$  of the radial view fit therefore provided additional discrimination against beam-halo muons. Showers with  $\chi_R^2/E > 0.1$  GeV $^{-1}$  (where  $E$  represents the shower energy) were excluded from the photon sample.

Distributions of  $P_T^{\text{away}}/p_T$ ,  $\delta$ , and  $\chi_R^2/E$  are shown in Fig. 6 for a beam-halo muon enriched sample (left) and a photon enriched sample (right). The rejection criteria discussed above suppressed beam-halo muon-induced background while having little impact upon the signal. The effect of these rejection criteria on the physics signal

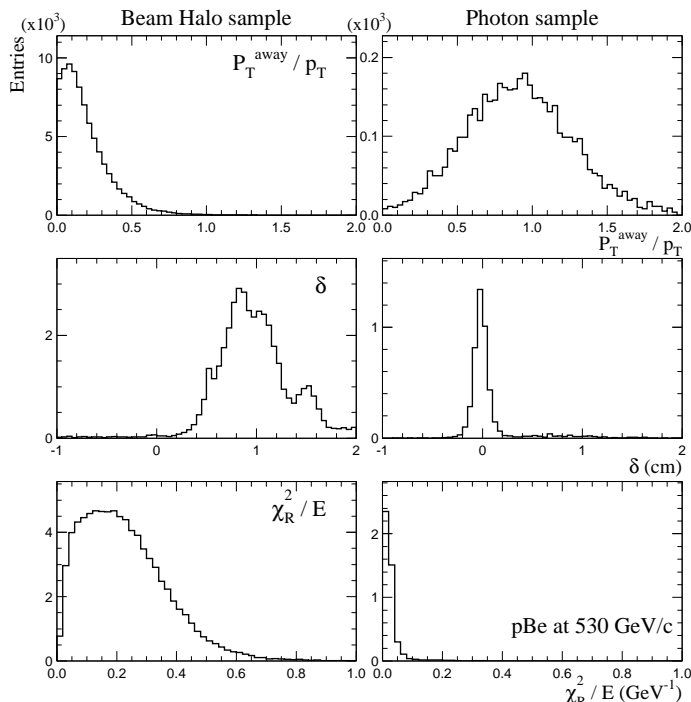


FIG. 6: Distributions in  $P_T^{away}/p_T$ ,  $\delta$ , and  $\chi_R^2/E$  for showers from beam-halo muons (left) and photons (right) with  $p_T > 5$  GeV/c. The beam-halo muon sample was obtained by requiring signals from the VW quadrant shadowing the reconstructed shower. The photon sample was obtained by imposing all the standard beam-halo muon rejection criteria with the exception of the requirement on the variable plotted.

was checked using more restrictive selection criteria. The fraction of signal lost by the application of each of the muon-rejection criteria provided a measure of the signal efficiency of these criteria. The application of the muon rejection criteria is estimated to result in the loss of  $\approx 7\%$  of the direct photons at  $p_T = 4$  GeV/c, and  $\approx 4\%$  at  $p_T = 7$  GeV/c, for the 530 and 800 GeV/c beam data. The corresponding losses for the 515 GeV/c  $\pi^-$  beam data are estimated to be 12% and 8% at  $p_T = 4$  and 7 GeV/c, respectively. Corrections for these losses, which are functions of  $p_T$  and  $y_{cm}$ , have been included in the results reported in this paper.

### E. Direct-photon candidates

The most significant source of direct-photon background is the electromagnetic decay of hadrons such as  $\pi^0$ 's and  $\eta$ 's. Photons were rejected from the direct-photon candidate sample if they combined with another photon in the same EMLAC octant to form a  $\gamma\gamma$  pair with invariant mass,  $M_{\gamma\gamma}$ , in the  $\pi^0$  or  $\eta$  mass region and with energy asymmetry,  $A_{\gamma\gamma} = |E_{\gamma_1} - E_{\gamma_2}| / (E_{\gamma_1} + E_{\gamma_2})$ , less than the value specified for each direct-photon candidate definition (described below). The residual background

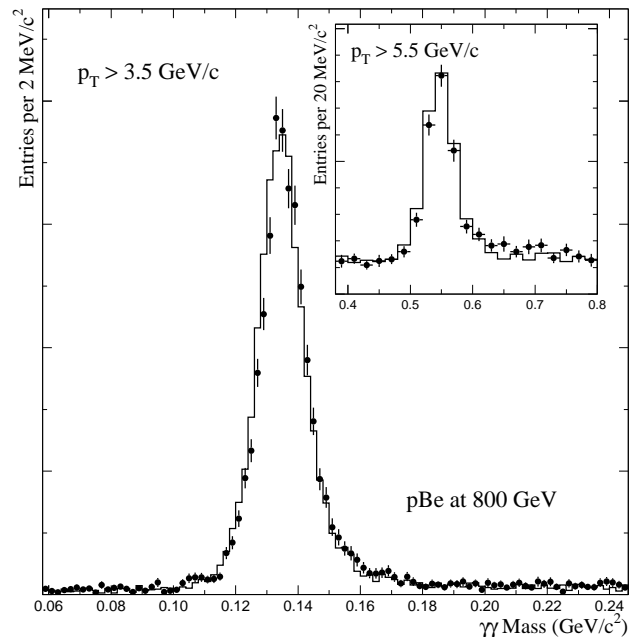


FIG. 7:  $\gamma\gamma$  mass distributions in the  $\pi^0$  and  $\eta$  (inset) mass regions for photon pairs with  $A_{\gamma\gamma} \leq 0.75$  and that satisfy the specified minimum  $p_T$  requirement in the data (histograms) compared to the results of the detailed detector simulation ( $\bullet$ ). The distributions have been normalized to the same area.

from these mesons, as well as from other sources of background, was evaluated using Monte Carlo samples that contained no generated direct photons.

In the neutral meson analyses [10, 11], a  $\pi^0$  candidate was defined as a combination of two photons with  $A_{\gamma\gamma} \leq 0.75$  detected within the fiducial region of the same EMLAC octant with  $100 < M_{\gamma\gamma} < 180$  MeV/c<sup>2</sup>;  $\eta$  candidates were similarly defined with  $450 < M_{\gamma\gamma} < 650$  MeV/c<sup>2</sup> (Fig. 7). The energy asymmetry requirement reduces uncertainties due to low energy photons. Background subtracted energy asymmetry distributions for photons in the  $\pi^0$  mass region are shown in Fig. 8. Combinatorial backgrounds under the peak regions in the mass distributions were evaluated using sideband subtraction.

Three direct-photon candidate definitions were used in this analysis: 75N, 90N, and 75S, which differed in the treatment of the background due to the decays of  $\pi^0$  mesons (the largest source of background). Corrections and backgrounds were calculated independently for each definition. In the 75N (90N) definition, any photon that formed a combination with another photon in the same EMLAC octant with  $M_{\gamma\gamma}$  in the  $\pi^0$  mass region and  $A_{\gamma\gamma} \leq 0.75$  ( $A_{\gamma\gamma} \leq 0.9$ ), was eliminated from the direct-photon candidate sample. A photon was also rejected if it formed a  $\gamma\gamma$  pair with another photon in the same octant with invariant mass in the  $\eta$  mass region with  $A_{\gamma\gamma} \leq 0.8$ .

The third definition, 75S, rejected the same photons as the 75N definition. However, photons that formed mass

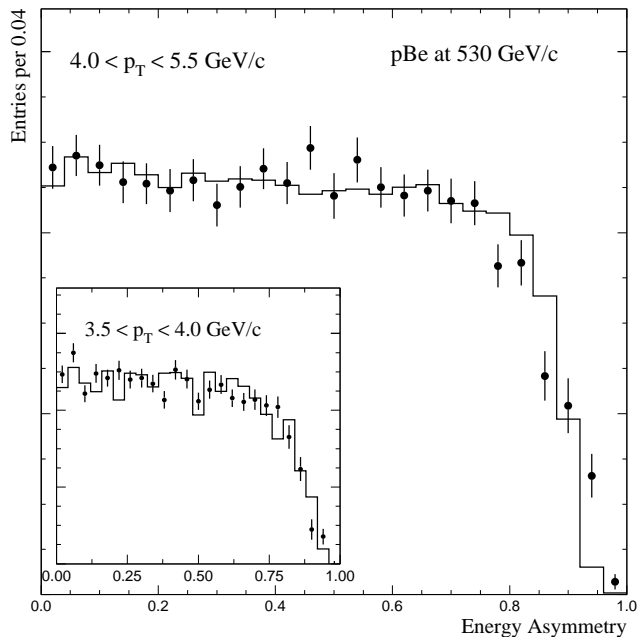


FIG. 8: Comparison of the side-band subtracted energy asymmetry distribution for photons from reconstructed  $\pi^0$  decays in data (histogram) and the detailed detector simulation ( $\bullet$ ). Comparisons for two  $p_T$  intervals,  $4.0 < p_T < 5.5$  GeV/ $c$  and  $3.5 < p_T < 4.0$  GeV/ $c$  (inset) are shown. The distributions have been normalized to the same area.

combinations with other photons in the  $\pi^0$  and  $\eta$  side-band regions were included with a weight of 2 (when these photons were in the same octant) to explicitly account for direct-photon losses due to accidental combinations under the  $\pi^0$  and  $\eta$  mass peaks. The 75N and 90N results both rely on the detailed simulation to account for the accidental losses of direct photons due to mass combinations with other photons that happen to land in the  $\pi^0$  or  $\eta$  mass windows.

Each of these definitions have relative strengths and weaknesses. The 90N definition rejects the most background, however, the residual background in this definition is more sensitive to the simulation of the low energy photons from  $\pi^0$  decay, which cause the losses at high  $A_{\gamma\gamma}$ . Additionally, accidental direct-photon losses are largest for this definition and must be accounted for by the simulation. The 75N and 75S definitions are less sensitive to the details of the low energy photon simulation, but lead to larger background levels. Comparing the fully corrected results using three definitions provided insights into the systematic uncertainties associated with the direct-photon cross-section measurements.

## F. Detailed detector simulation

The Meson West spectrometer was modeled using a detailed GEANT [28] simulation (DGS). The simulated particles in the generated events were propagated through

the GEANT model of the spectrometer and interacted appropriately. Simulated showers in the EMLAC were parameterized once the energies of the interacting particles were  $< 10$  MeV. A preprocessor converted GEANT information into the hits and strip energies simulating the detailed response of the various detectors. The preprocessor simulated hardware effects such as channel noise and gain variations.

Single particle distributions, reconstructed data events, and the HERWIG v5.6 [29] event generator were employed as inputs to the detailed GEANT simulation. The direct-photon background studies were carried out primarily using samples of HERWIG  $2 \rightarrow 2$  QCD hard parton scatters (IPROC=1500). No direct photons were included in these samples. The detailed simulations were used to evaluate contributions to the direct-photon background from numerous sources including  $\pi^0$ ,  $\eta$ ,  $\omega$ ,  $\eta'$ ,  $K_L^0$ ,  $K_S^0$ ,  $e^\pm$ , neutrons and charged pions.

Generated events were processed through the reconstruction software used for the data analysis. This technique accounted for inefficiencies and biases in the reconstruction algorithms. Additional information on the detailed simulation of the Meson West spectrometer can be found elsewhere [10, 30].

The simulated HERWIG events were weighted (in an iterative fashion) so that the resulting  $\pi^0$  spectra agreed with our measured cross sections as functions of  $p_T$  and  $y_{cm}$  [10, 11]. As a result, the final corrections were based on the shape of the spectra from data rather than on the HERWIG event generator [30]. Similarly, the generated  $\eta$ 's were weighted so that the resulting simulated production spectra were consistent with our measured  $\eta/\pi^0$  results [31]. HERWIG v5.6 was assumed to reproduce other particle spectra after these were weighted by the results of the fits to the  $\pi^0$  data [32, 33]. Photons reconstructed in the background samples that satisfied the direct-photon candidate requirements,  $\gamma_{bckg}$ , were assigned the weighting appropriate to their identified parent.

Figure 7 shows  $\gamma\gamma$  mass spectra in the  $\pi^0$  and  $\eta$  mass regions compared to the results of the detailed GEANT simulation. In addition to demonstrating that the DGS simulated the EMLAC resolution well, the agreement between the levels of combinatorial background indicates the DGS provided a reasonable simulation of the underlying event structure. Figure 8 shows a comparison between the DGS results and the data for the  $\pi^0$  energy asymmetry after side-band subtraction. This figure illustrates that the simulation accurately describes the losses of low energy photons.

The direct-photon reconstruction efficiency was evaluated using a dedicated sample of HERWIG-generated direct-photon events. Reconstruction inefficiencies for direct photons were relatively small over most of the kinematic range (Fig. 9).

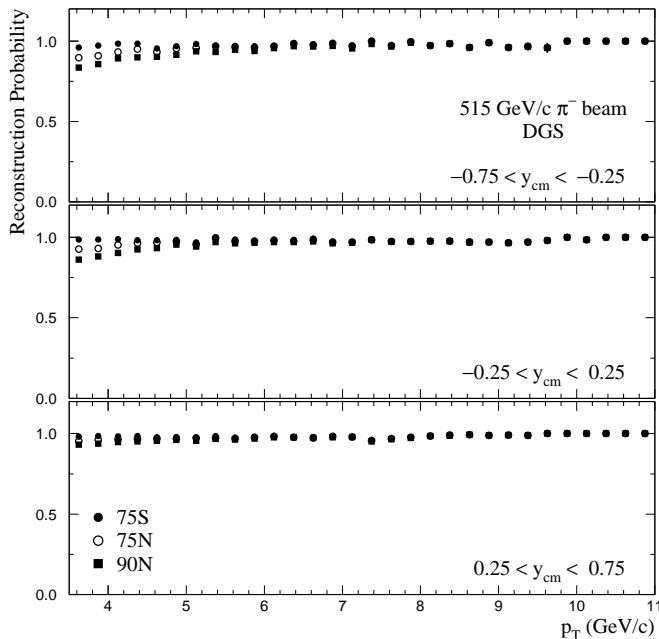


FIG. 9: Probabilities to reconstruct direct photons using the 75S, 75N, and 90N definitions as functions of generated  $p_T$  of the photons for several rapidity ranges as determined via the detailed GEANT simulation.

### G. EMLAC energy scale

The calibration of the EMLAC response was based on the reconstructed masses of  $\pi^0$  mesons in the  $\gamma\gamma$  decay mode and verified using  $\eta$ 's,  $\omega$ 's, converted photons ( $e^+e^-$ ), and  $J/\psi$ 's [19, 34]. The steeply falling  $\pi^0$   $p_T$  spectrum, combined with the calorimeter's resolution, results in a small offset (1%) in the mean reconstructed photon energies when plotted as a function of the generated  $p_T$  (Fig. 10). To account for this offset and for potential biases in the calibration procedure, the simulated EMLAC was calibrated in the same manner as the real detector. The impact of detector resolution on the energy scale calibration and on the production spectra was incorporated into the Monte Carlo based corrections [30]. The simulation was also employed to evaluate the mean correction for energy deposited in the material upstream of the EMLAC. Two-photon mass distributions in the  $\pi^0$  and  $\eta$  mass regions from both data and DGS events after energy scale calibration are illustrated in Fig. 7.

The energy scale calibration was also verified to be appropriate for direct photons. This is important since the EMLAC energy response was sensitive to event structure; direct photons are expected to be more isolated than corresponding photons from meson decays since the mesons are frequently accompanied by other jet particles. The single photon energy scale was verified with  $\eta \rightarrow \gamma\gamma$  where the photons were widely separated, as well as with isolated electrons, and the DGS. Figure 10 displays a comparison of the ratio between reconstructed and gen-

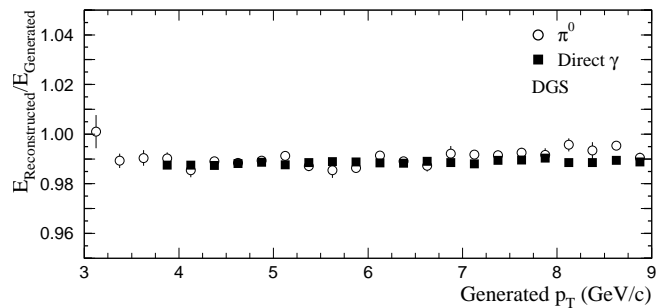


FIG. 10: Ratios of reconstructed to generated energy for  $\pi^0$ 's and direct photons as functions of their generated  $p_T$  values as determined via detailed GEANT simulations. The small offset from 1.0 is due to the combined effects of the steeply falling particle production spectra and the EMLAC resolution.

erated energy as functions of generated  $p_T$  for  $\pi^0$ 's and direct photons from the DGS. Cuts were applied to both the photons from  $\pi^0$  decay and direct photons ensuring equal treatment by the reconstruction software [34]. These two distributions agree well.

### H. Direct-photon background

The residual background to the direct-photon signal from  $\pi^0$ 's and  $\eta$ 's, as well as from other (previously mentioned) sources, was calculated by applying the 75N, 90N, and 75S photon definitions to DGS samples that contained no generated direct photons. Ratios of the resulting  $\gamma_{bckg}$  to the measured  $\pi^0$  cross sections [10, 11] are shown as functions of  $p_T$  for interactions on the beryllium target in Fig. 11. As indicated in the section describing the various direct-photon candidate definitions, the 90N background level is substantially lower than the 75N and 75S background levels.

Figure 12 shows the  $\gamma_{bckg}/\pi^0$  for several  $y_{cm}$  intervals for the simulated 530 GeV/c  $p$ Be interactions. The shapes of the background are quite similar in the backward and central  $y_{cm}$  regions. However, at forward  $y_{cm}$  and high  $p_T$  the contribution to the background due to coalesced photons from  $\pi^0$  decays is clearly visible. The  $\gamma_{bckg}/\pi^0$  were fitted to functions in  $p_T$  and  $y_{cm}$ . Projections from the fits are indicated by the curves in Figs. 11 and 12.

### I. Parameterized detector simulation

A second Monte Carlo simulation of detector effects (PMC) was used to cross check the DGS and for large statistics studies. This simulation employed parameterizations of physics cross sections and detector responses [30, 34]. The inclusive  $\pi^0$  and direct-photon cross sections were parameterized as two-dimensional functions



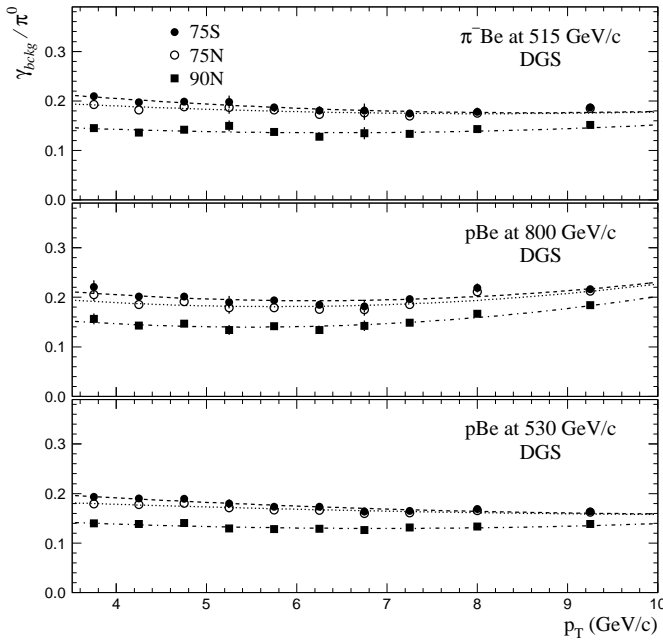


FIG. 11:  $\gamma_{bckg}/\pi^0$  for each direct-photon candidate definition as a function of  $p_T$  based upon analysis of DGS samples excluding the direct-photon samples. The points represent the binned results; the curves represent fits to these backgrounds integrated over rapidity.

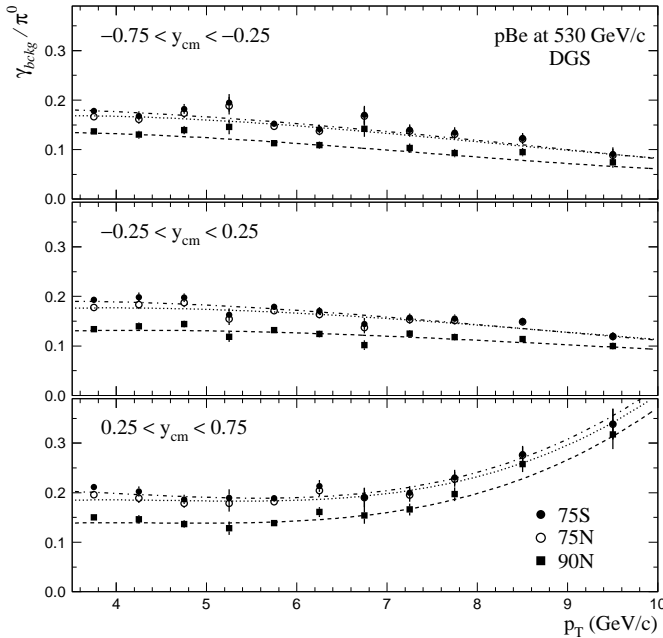


FIG. 12:  $\gamma_{bckg}/\pi^0$  for each direct-photon candidate definition as a function of  $p_T$  for backward, central, and forward rapidities based upon analysis of DGS samples excluding the direct-photon samples. The curves represent the results of the background fits integrated over the indicated rapidity range.

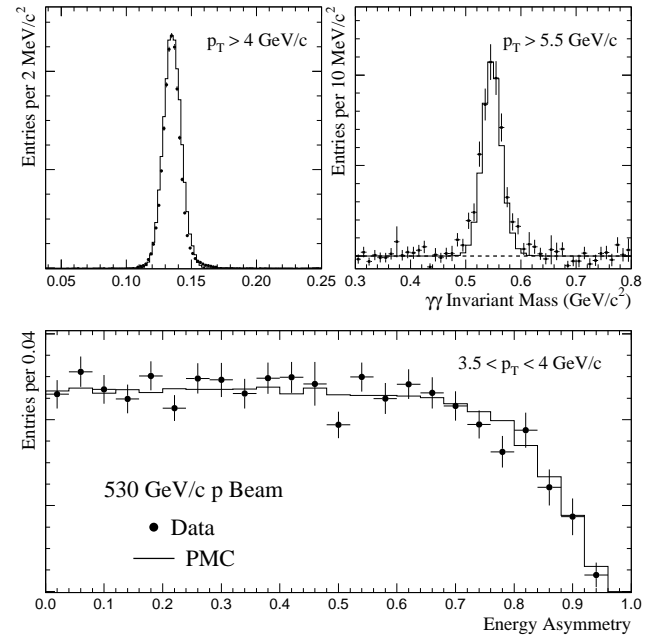


FIG. 13: Top: comparison between background-subtracted  $\gamma\gamma$  mass distributions for data ( $\bullet$ ) and the PMC (histogram) for photon pairs with  $A_{\gamma\gamma} \leq 0.75$  in the  $\pi^0$  and  $\eta$  mass regions. Note that the background levels are centered on zero (dashed line) in the data mass plots due to the background subtraction. Bottom: comparison of the corresponding energy asymmetry distributions for  $\gamma$ 's from  $\pi^0$  decays. The distributions have been normalized to the same area.

in  $p_T$  and  $y_{cm}$  [30]. The  $\eta$ ,  $\omega$ , and  $\eta'$  cross sections were represented using values consistent with our measured  $\eta/\pi^0$  [10, 11, 31],  $\omega/\pi^0$  [13], and using  $\eta'/\pi^0=0.85$ , as indicated in Ref. [35] (after accounting for the updated  $\eta' \rightarrow \gamma\gamma$  branching ratio [36]).

An interaction vertex was generated in the simulated target for every event (Fig. 3). This primary vertex distribution was used to ensure the simulated photons traversed the proper amount of material. Generated mesons were allowed to decay into final state particles. Photons were allowed to convert into  $e^+e^-$  pairs when appropriate; the energy of the resulting electrons was reduced using the GEANT function for bremsstrahlung radiation. Electron four-vectors were smeared for multiple scattering in the target region and the resolution of the tracking system, and adjusted to account for the impulse due to the magnet. The parameters of the photons that did not convert were smeared to account for energy and position resolution [19]. Figure 13 displays a comparison between  $\gamma\gamma$  mass distributions from the PMC and the background-subtracted data in the  $\pi^0$  and  $\eta$  mass regions as well as the energy asymmetry distribution for photons from  $\pi^0$  decays. As illustrated by these plots, the PMC provides a reasonable characterization of the data.

The PMC was used to identify contributions to the direct-photon background. Photons from  $\pi^0 \rightarrow \gamma\gamma$  decays with  $A_{\gamma\gamma}$  greater than required by the relevant

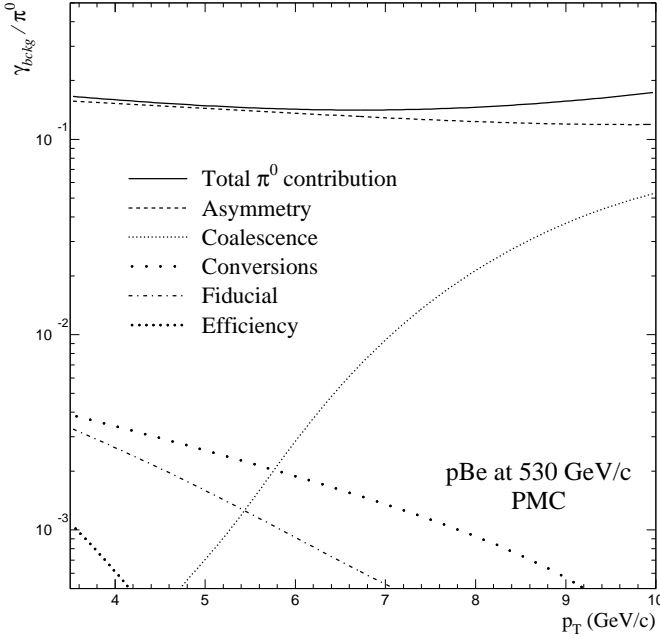


FIG. 14: Contribution to  $\gamma_{bckg}/\pi^0$  from  $\pi^0$  decays for the 75S photon definition evaluated via the PMC. Also shown are the contributions from each of the categories described in the text.

photon definition were the dominant contribution to the background. However, photons from  $\pi^0$  decays with smaller  $A_{\gamma\gamma}$  also contribute to  $\gamma_{bckg}$  when the other photon is lost. Hence, the remainder of the photons from  $\pi^0$  decays were classified according to our ability to detect both photons from the  $\pi^0$  decay. The photons were projected to the front face of the EMLAC. If one was outside the EMLAC fiducial volume while the other was within that fiducial volume, then the latter contributed to  $\gamma_{bckg}$ . In addition, photons that landed in different EMLAC octants were classified as background candidates. Contributions to  $\gamma_{bckg}$  from photon conversions and detector inefficiencies were obtained from the sample when both photons landed within a single EMLAC octant. Each photon was assigned a weight based on the conversion probability of the other photon. The  $\gamma_{bckg}$  contribution from detector inefficiencies was determined by weighting each photon by the non-detection probability for the other photon. Double counting between these sources was eliminated by applying the non-conversion probability of the undetected photon to each  $\gamma_{bckg}$  contribution. Since the  $\gamma_{bckg}$  were required to be inside the fiducial volume, the impact of the EMLAC acceptance was properly taken into account.

The DGS was used to assess the coalescence probability function as the coalescence of two photons from a  $\pi^0$  decay into a single reconstructed shower depended on many factors including the relative geometry of the two photons, their total and relative energies, and the ability of the reconstructor to resolve the photons. Background contributions from this source were assigned the  $\pi^0$  en-

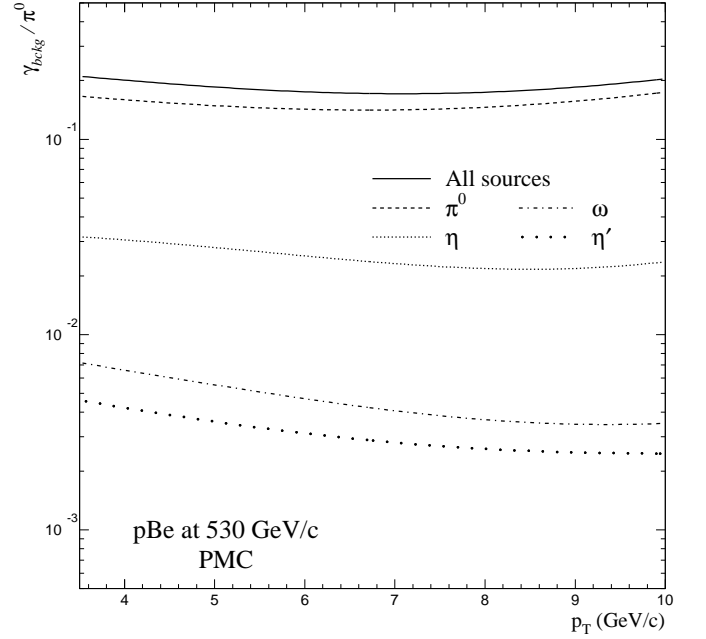


FIG. 15: Contribution to  $\gamma_{bckg}/\pi^0$  from  $\pi^0$ 's,  $\eta$ 's,  $\omega$ 's, and  $\eta$ 's for the 75S photon definition as evaluated using the PMC.

ergy and weighted by the non-conversion probability and detection efficiency of each photon and the acceptance of the higher energy photon.

The ratio of  $\gamma_{bckg}$  from  $\pi^0 \rightarrow \gamma\gamma$  decays to generated  $\pi^0$ 's is shown in Fig. 14 for incident 530 GeV/c  $p$  beam on the beryllium targets. The contributions from each of the categories described above are also shown in the same figure. It is evident from the figure that photons resulting from highly asymmetric  $\pi^0$  decays are the dominant contribution to the direct-photon background, although, at very high  $p_T$ , the coalescence contribution is also significant.

The background contribution from the decay  $\eta \rightarrow \gamma\gamma$  was evaluated in an analogous manner. Photons from  $\eta$  decays with energy asymmetry  $A_{\gamma\gamma} > 0.8$  were included in the direct-photon background. Photons from the decays  $\omega \rightarrow \pi^0\gamma$ ,  $\eta' \rightarrow \rho\gamma$ ,  $\eta' \rightarrow \omega\gamma$ ,  $\eta' \rightarrow \gamma\gamma$ , and  $\pi^0 \rightarrow \gamma e^+e^-$  were also evaluated as potential contributors to  $\gamma_{bckg}$ . Photons arising from the subsequent decay of the  $\pi^0$  in the case of the  $\omega$  decay and the  $\rho \rightarrow \pi^0\pi^0$  decays were not considered since those contributions were already included in the simulation of the inclusive  $\pi^0$  sample. The background contribution from the  $e^+e^-$  pair in  $\pi^0 \rightarrow \gamma e^+e^-$  decays was negligible due to the small branching ratio for this decay mode combined with the typically significantly lower  $p_T$  of the daughter electrons relative to the parent  $\pi^0$ . Furthermore, most electrons were rejected by the distance-to-nearest-track requirement (Fig. 5).

The total  $\gamma_{bckg}/\pi^0$  as determined using the PMC is shown in Fig. 15 for incident 530 GeV/c  $p$  on beryllium. The contribution to  $\gamma_{bckg}/\pi^0$  due to each of the particles

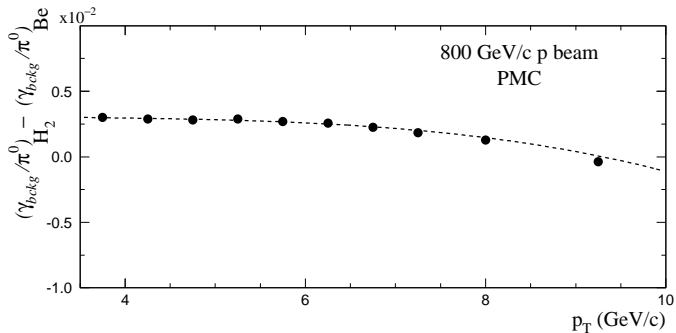


FIG. 16: Difference between  $\gamma_{bckg}/\pi^0$  for the hydrogen and beryllium targets as a function of  $p_T$  as determined via the PMC. The dashed curve represents a fit to this difference.

considered in the PMC is also shown in that figure. The contribution from  $\eta$  decays is roughly 20% of the  $\pi^0$  contribution, as expected from simple considerations of the  $\eta$  and  $\pi^0$  production rates [10, 11] and their respective two-photon branching ratios [36].

#### J. Direct-photon background for hydrogen target data

Fits to  $\gamma_{bckg}/\pi^0$  evaluated using the DGS were only made for the beryllium target due to relatively poor DGS statistics in the other targets. However,  $\gamma_{bckg}/\pi^0$  is expected to be slightly different for each target due to the different amounts of target material the photons must traverse. A correction to  $\gamma_{bckg}/\pi^0$  was therefore evaluated using the PMC. The difference between  $\gamma_{bckg}/\pi^0$  on the hydrogen and beryllium targets is shown for the 800 GeV/c proton beam sample in Fig. 16. The corresponding results are similar for the other incident beams. Note that the difference is small ( $< 0.003$ ) but positive at low  $p_T$  because the conversion background contribution is larger for the more upstream hydrogen target. However, at high  $p_T$ , the correction becomes very slightly negative because the contribution due to coalescence is reduced by the additional photon conversions. The target differences were fit as functions of  $p_T$  and  $y_{cm}$  for each incident beam and applied as additive corrections to the nominal  $\gamma_{bckg}/\pi^0$  fit obtained using the DGS and the beryllium target.

#### K. Background subtraction uncertainties

The systematic uncertainty in the background subtraction was estimated via the sensitivity of the results to the various direct-photon definitions and to variations in the size of the  $\pi^0$  and  $\eta$  side-band regions and via detailed studies of the Monte Carlo simulations. Ratios of direct-photon cross sections obtained using the different candidate definitions are displayed in Fig. 17 for all three incident-beam samples. These ratios generally dif-

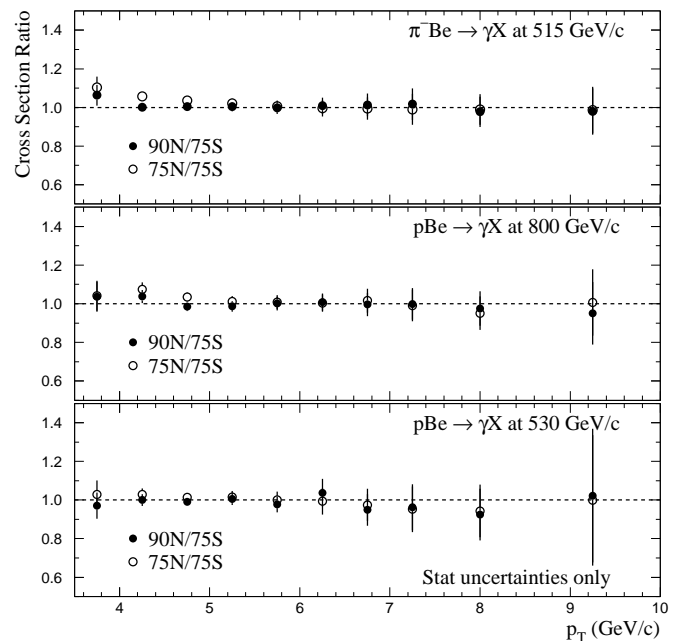


FIG. 17: Ratios between direct-photon cross sections evaluated using the 90N and 75S direct-photon candidate definitions as functions of photon  $p_T$  for the three major incident beams. Ratios between direct-photon cross sections evaluated using the 75N and 75S direct-photon candidate definitions are also shown.

fered from unity by  $< 5\%$ . This very good agreement between the direct-photon cross sections measured using these different definitions illustrates the robust nature of our results.

Comparisons between detailed and parameterized detector simulations provided increased confidence in our understanding of the direct-photon background since the two simulations represent essentially independent calculations of  $\gamma_{bckg}$ . The PMC-evaluated  $\gamma_{bckg}$  is based on relatively simple considerations and included only the major background sources. Special runs of the DGS were performed limiting the background sources to those included in the PMC.  $\gamma_{bckg}/\pi^0$  from the restricted background source DGS and the PMC are compared in Fig. 18. The two simulation results agree quite well.

Measured four-vectors from particles reconstructed in data events were also employed as inputs to the GEANT simulation. This provided an additional measure of the uncertainty associated with the modeling of the detector environment. A comparison of  $\gamma_{bckg}/\pi^0$  produced in the DGS using the weighted HERWIG event generator and reconstructed data events is shown in Fig. 19. Only background sources common to both simulations were included in the comparison. The  $\gamma_{bckg}/\pi^0$  results evaluated via these two methods are consistent.

The impact of uncertainty in  $\eta/\pi^0$  on  $\gamma_{bckg}/\pi^0$  was determined using the PMC. The values used for  $\eta/\pi^0$  were shifted by  $\pm 0.04$ ; these shifts resulted in a  $\pm 1.5\%$  change in  $\gamma_{bckg}/\pi^0$ .

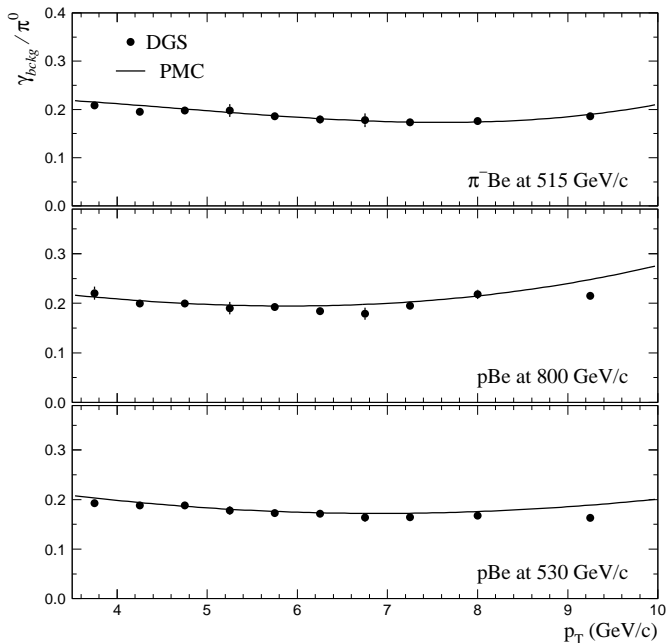


FIG. 18: Comparison of  $\gamma_{bckg}/\pi^0$  between the restricted background source DGS ( $\bullet$ ) and the PMC (curve) for each of the three major incident beam configurations for the 75S photon definition.

### L. Normalization

Electronic scalers that counted signals from the beam hodoscope and beam hole counters were used to establish the number of beam particles incident on the target. Other scalers logged the state of the trigger and data acquisition system. Information from these scalers was used to determine the number of beam particles incident upon the spectrometer when it was ready to record data. Small corrections for multiple occupancy in the beam hodoscope and for absorption of beam in the target material were included in the normalization.

Additional discussion on the normalization including details regarding independent normalization methods and cross checks can be found elsewhere [10, 11]. The net systematic uncertainty in the overall normalization is 8%. This evaluation is based upon several considerations: the good agreement between results from the independent normalization methods, the stability of the cross section results from various sections of the data, the internal consistency of the scalers, and a detailed analysis of the design, implementation, and performance of the trigger.

### M. Secondary beam contamination

The Meson West beamline transported 0.8 TeV/c primary protons from the Fermilab Tevatron and 0.5 TeV/c secondary beams of both polarities. The 800 GeV/c pri-

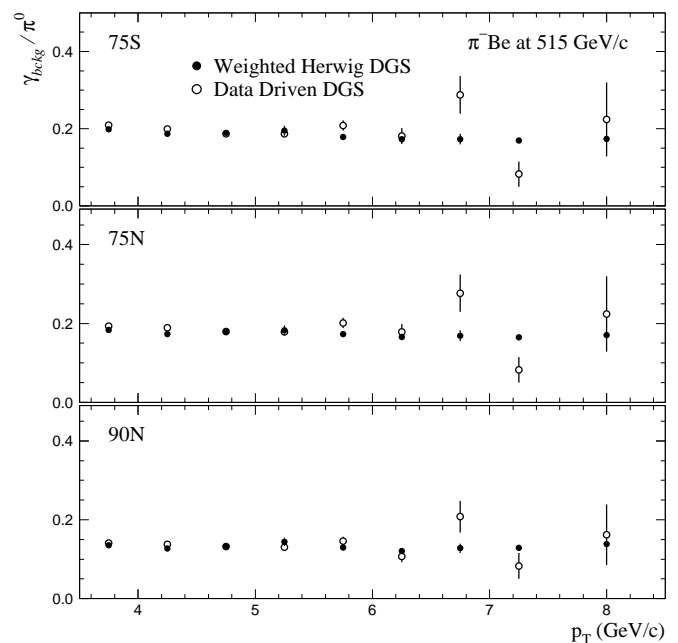


FIG. 19: Comparison of  $\gamma_{bckg}/\pi^0$  from the DGS using weighted HERWIG events and using reconstructed data inputs as the event generators for the 75S, 75N, and 90N direct-photon candidate definitions.

mary beam has a negligible momentum spread. The negative secondary pion beam was determined to have a mean momentum of  $515 \pm 2$  GeV/c with an estimated halfwidth of 30 GeV/c. The secondary proton beam was determined to have a mean momentum of  $530 \pm 2$  GeV/c and similar momentum spread. This momentum spread in the secondary beams introduces a small uncertainty ( $< 4\%$ ) in comparisons with theory evaluated at the mean beam momentum.

The minority particle fractions in the 530 GeV/c positive secondary beam were measured using the beamline Čerenkov detector to be 2.75%  $\pi^+$  and 0.5%  $K^+$  [24]. Analysis of the 515 GeV/c negative secondary beam indicated 1%  $K^-$  component, and negligible  $\bar{p}$  content.

The direct-photon cross sections for incident 530 GeV/c  $p$  beam have been corrected for the small incident pion contamination as follows. An estimate of the direct-photon cross section from incident  $\pi^+$  was generated from a product of our measured incident  $\pi^-$  cross sections and the ratio of next-to-leading-order PQCD calculations [37, 38] for direct-photon production in  $\pi^+$  and  $\pi^-$  beams to account for the differences in incident quark content. The direct-photon cross sections reported here for incident 530 GeV/c protons were corrected to account for the minority pions using this estimate of the direct-photon cross section from incident  $\pi^+$  combined with the measured incident minority particle fraction. The correction was  $< 1\%$  at  $p_T = 4$  GeV/c and  $< 5\%$  at  $p_T = 8$  GeV/c.

The direct-photon cross-section measurements have not been corrected for the incident kaon contributions

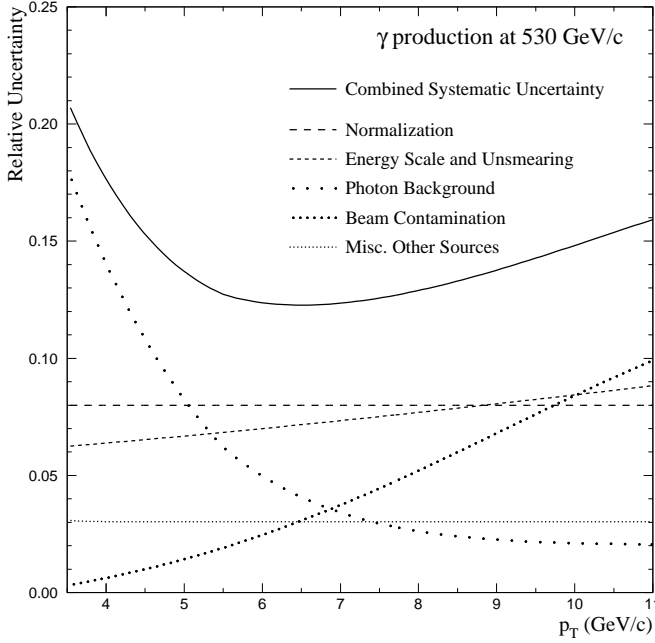


FIG. 20: Relative systematic uncertainty for the direct-photon cross section as a function of  $p_T$  for incident 530 GeV/c protons.

due to the lack of an incident kaon PDF. The potential bias from this source was studied using restrictive cuts based upon the Čerenkov detector data and the impact of the kaon contamination upon the reported cross-section measurements is expected to be negligible.

#### N. Summary of systematic uncertainties

The principal contributions to the systematic uncertainty in the direct-photon cross-section results arose from the following sources: normalization, background subtraction, the calibration of photon energy response and detector-resolution unsmearing, and incident beam contamination (for the 530 GeV/c  $p$  beam). Other sources of uncertainty, which contributed at the one to two percent level, included: photon reconstruction, beam-halo muon rejection, geometric acceptance, photon conversions, trigger response, and vertex finding. The relative systematic uncertainty in the direct-photon cross section is presented as a function of  $p_T$  in Fig. 20 for the 530 GeV/c  $p$ Be data. With the exception of the beam contamination contribution, the corresponding uncertainties for the other measurements are similar. The total systematic uncertainties, combined in quadrature, are quoted with the cross sections in the appropriate tables. Note that some of these contributions to the systematic uncertainty (e.g. normalization) are strongly correlated between bins.

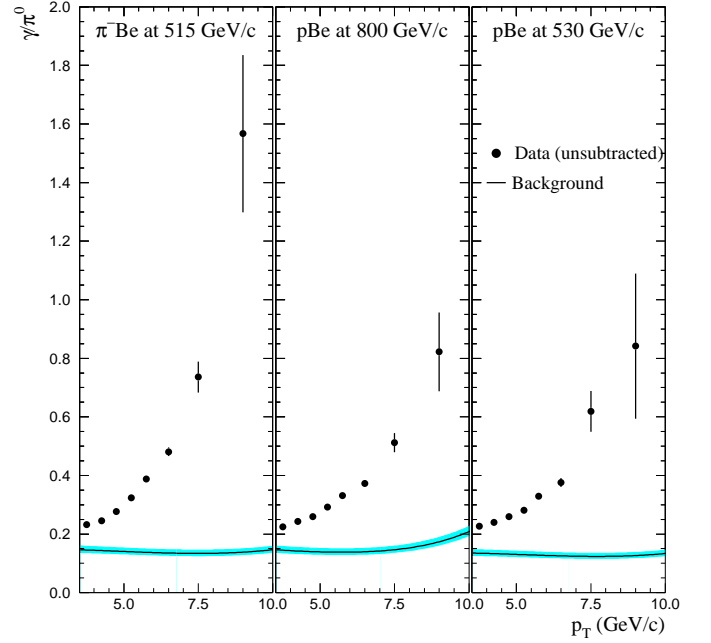


FIG. 21: Ratios of the 90N direct-photon candidate spectra to the measured  $\pi^0$  cross sections (points) compared to  $\gamma_{bkg}/\pi^0$  from the DGS (curves) as functions of  $p_T$  for the data samples considered in this paper. The error bars represent statistical contributions to the uncertainties. The width of each band around the background represents the systematic uncertainty on that background.

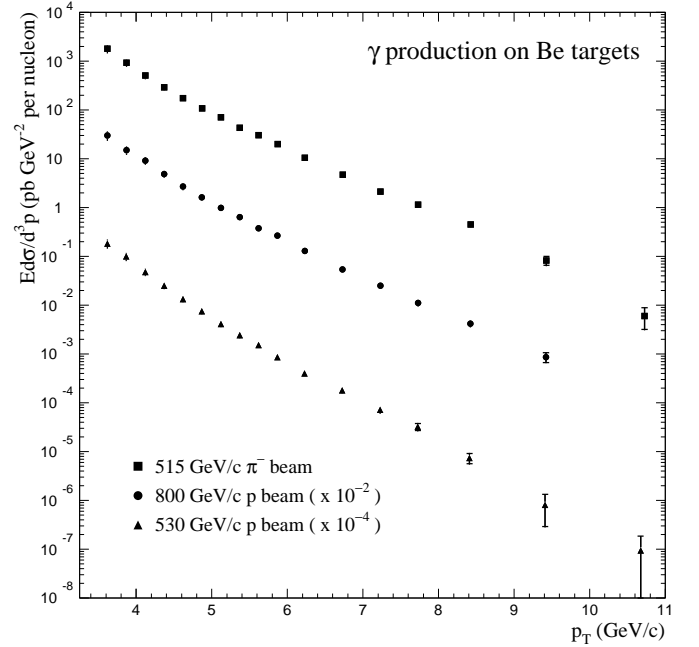


FIG. 22: Invariant differential cross sections per nucleon for direct-photon production as functions of  $p_T$ , averaged over rapidity, for 515 GeV/c  $\pi^-$  and 800 and 530 GeV/c proton beams incident upon beryllium. The error bars represent the statistical and systematic uncertainties combined in quadrature; the innermost interval indicates the statistical uncertainties.

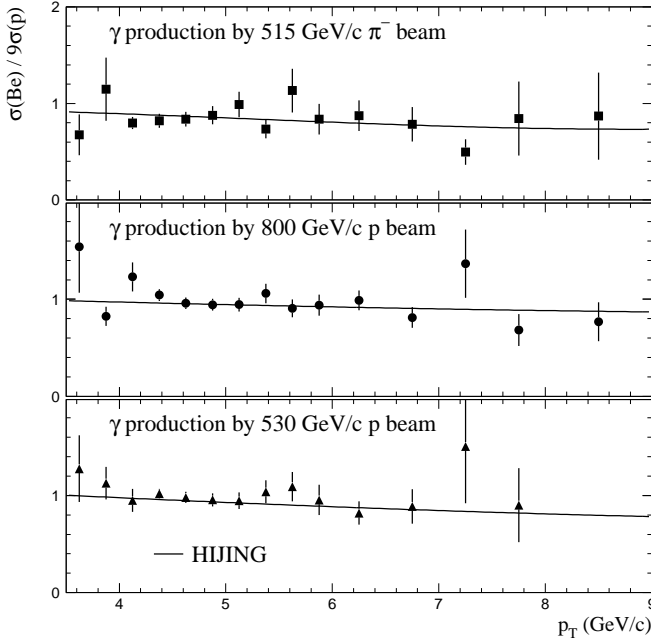


FIG. 23: Ratios of inclusive direct-photon production per nucleon in  $p\text{Be}$  to those in  $pp$  collisions as functions of photon  $p_T$ , compared with curves representing predictions from HIJING. The error bars represent only statistical contributions to the measurement uncertainties.

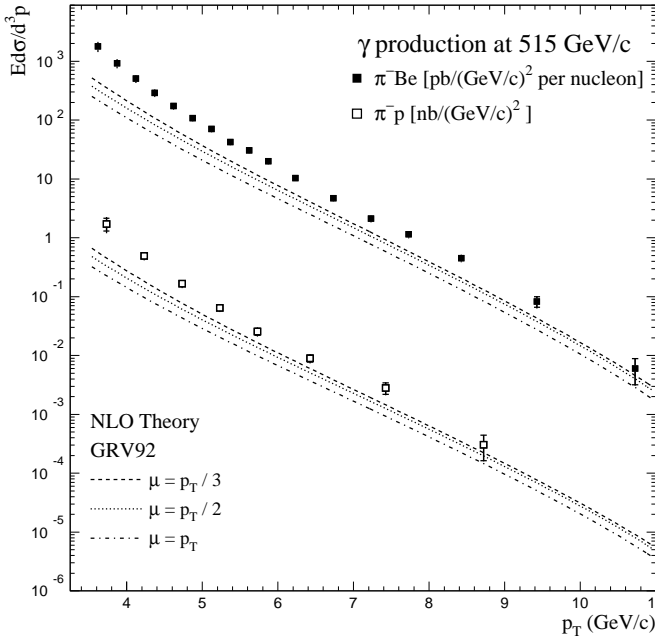


FIG. 24: Invariant differential cross sections per nucleon for direct-photon production as functions of  $p_T$  in  $\pi^- \text{Be}$  and  $\pi^- p$  interactions at 515 GeV/c. The error bars represent the statistical and systematic uncertainties combined in quadrature; the innermost interval indicates the statistical uncertainties. Overlaid on the data are NLO PQCD results for three choices of the factorization and renormalization scales.

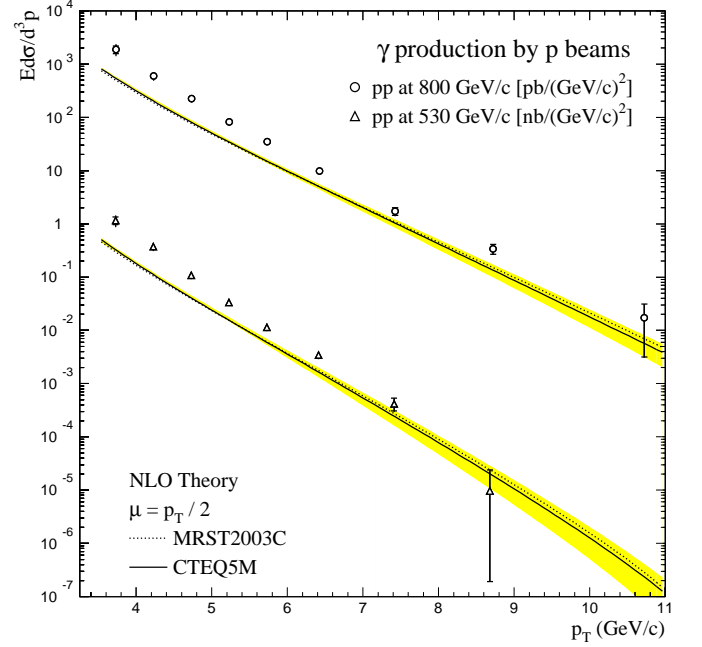


FIG. 25: Invariant differential cross sections per nucleon for direct-photon production as functions of  $p_T$  in  $pp$  interactions at 800 and 530 GeV/c. The error bars represent the statistical and systematic uncertainties combined in quadrature; the innermost interval indicates the statistical uncertainties. Overlaid on the data are NLO PQCD predictions for the CTEQ5M and MRST2003C PDF; the band illustrates the PDF uncertainty estimated via the MRST2001E set.

## IV. RESULTS AND DISCUSSION

### A. Results

The ratios of the  $90N$  direct-photon candidate spectra to the measured  $\pi^0$  cross sections [10, 11] as functions of  $p_T$  are compared to  $\gamma_{\text{bckg}}/\pi^0$  from the DGS in Fig. 21. All three samples are characterized by rapidly rising direct-photon signal to background ratios.

The direct-photon cross sections were extracted statistically using the fits to  $\gamma_{\text{bckg}}/\pi^0$ . The invariant differential cross sections per nucleon for direct-photon production from 515 GeV/c  $\pi^-$  and 800 and 530 GeV/c proton beams incident on beryllium are presented as functions of  $p_T$  in Fig. 22. Results from 515 GeV/c  $\pi^-$  and 530 GeV/c  $p$  beams are averaged over the rapidity range  $-0.75 \leq y_{\text{cm}} \leq 0.75$ ; results from the 800 GeV/c  $p$  beam are averaged over  $-1.0 \leq y_{\text{cm}} \leq 0.5$ . Data points are plotted at abscissas that correspond to the average value of the cross section in each  $p_T$  bin, assuming local exponential dependence on  $p_T$  [39]. The inclusive cross sections are tabulated in the Appendix (Tables I–VIII).

Ratios of the direct-photon cross sections per nucleon on beryllium to those on hydrogen are shown versus  $p_T$  in Fig. 23. The ratios are compared with results from the Monte Carlo program HIJING [40]. The results from

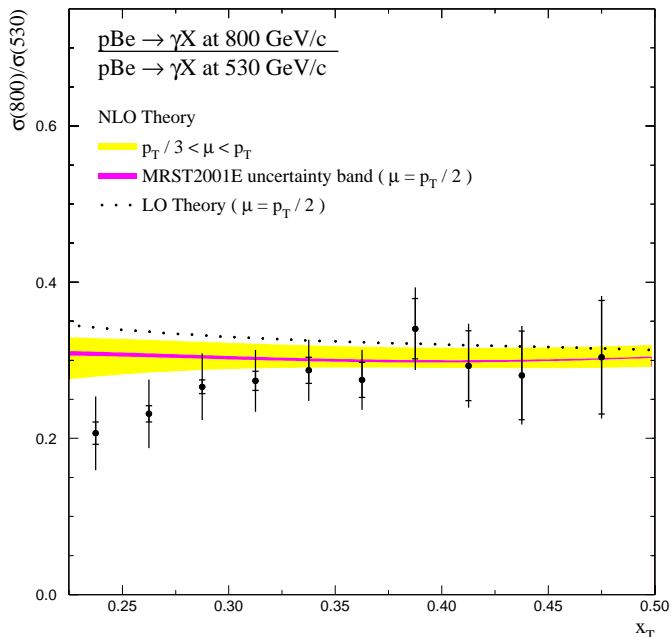


FIG. 26: The ratio of 800 GeV/c to 530 GeV/c proton beam direct-photon cross sections as a function of  $x_T$ . The error bars represent the statistical and systematic uncertainties combined in quadrature; the innermost interval indicates the statistical uncertainties. The dotted curve shows the results of LO PQCD calculations using the CTEQ5L PDF and  $\mu = p_T/2$ . Shaded bands illustrate the results from NLO PQCD calculations. The outer band is bounded by  $\mu = p_T/3$  and  $\mu = p_T$ ; the inner band by the uncertainty of the MRST2001E PDF set.

HIJING, which is designed to simulate particle production in  $pp$ ,  $pA$ , and  $AA$  collisions, are in good agreement with the data. The PQCD calculations described below for interactions on beryllium have been adjusted to account for nuclear effects using HIJING results.

## B. Comparisons with PQCD

Next-to-leading order (NLO) PQCD calculations [37, 38] using the GRV92 PDF [7] are compared to our measured direct-photon cross sections for incident  $\pi^-$  beam in Fig. 24. Theoretical results are presented for three choices of factorization scale:  $\mu = p_T$ ,  $p_T/2$ , and  $p_T/3$ . The renormalization scale was set equal to the factorization scale. Expectations for these choices of  $\mu$  lie significantly below the data, in addition to exhibiting a large dependence on choice of scale. Calculations that include higher-order effects, such as threshold resummation and certain NNLO diagrams [41–45] significantly reduce scale dependence relative to NLO calculations, and yield results comparable to the NLO calculation with  $\mu = p_T/2$ .

There is additional theoretical uncertainty associated with the choice of PDF. Recently published PDF provide individual fits for variations in fit parameters. Un-

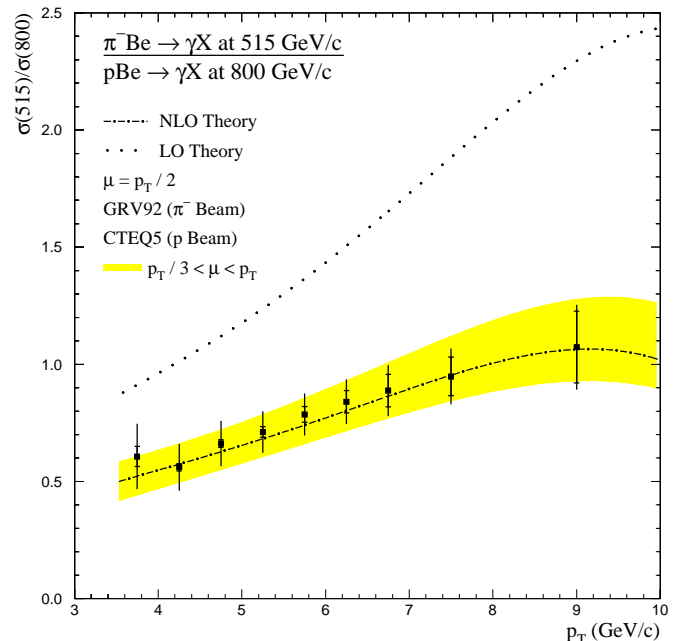


FIG. 27: The ratio of 515 GeV/c  $\pi^-$  beam to 800 GeV/c proton-beam direct-photon cross sections as a function of  $p_T$ . The error bars represent the statistical and systematic uncertainties combined in quadrature; the innermost interval indicates the statistical uncertainties. Results of LO PQCD calculations using  $\mu = p_T/2$  are represented by the dotted curve. The shaded band illustrates results from NLO PQCD calculations bounded by  $\mu = p_T/3$  and  $\mu = p_T$ .

certainty bands based upon these fits are presented in Fig. 25 for the MRST2001E PDF set [46, 47] compared with the  $pp$  data. We conclude there is insufficient flexibility in the PDF to accommodate the difference between theory and data.

Not surprisingly, NLO PQCD has reduced scale dependence and significantly improved agreement with data when compared to ratios of direct-photon cross sections. The ratio of the 800 to 530 GeV/c direct-photon cross sections is presented as a function of  $x_T = 2p_T/\sqrt{s}$  in Fig. 26. The ratio between 515 GeV/c  $\pi^-$  beam and 800 GeV/c proton-beam direct-photon cross sections as a function of  $p_T$  is shown in Fig. 27. The broad bands on the NLO theory in both figures are bounded by  $\mu = p_T/3$  and  $p_T$ ; the inner band in Fig. 26 represents the uncertainty attributed to the PDF. The dotted curves in both figures show the results of leading-order (LO) PQCD calculations for  $\mu = p_T/2$ . We chose  $x_T$  as the plotting variable in Fig. 26 to compensate for the different average parton-parton collision energies in the numerator and the denominator;  $p_T$  was used as the plotting variable in Fig. 27 since the average energy per colliding valence quark is already similar in the numerator and the denominator. There is relatively little difference between the LO and NLO curves in Fig. 26, where the beam particle types are the same for both the numerator and the denominator. In marked contrast, however, in Fig. 27, where the

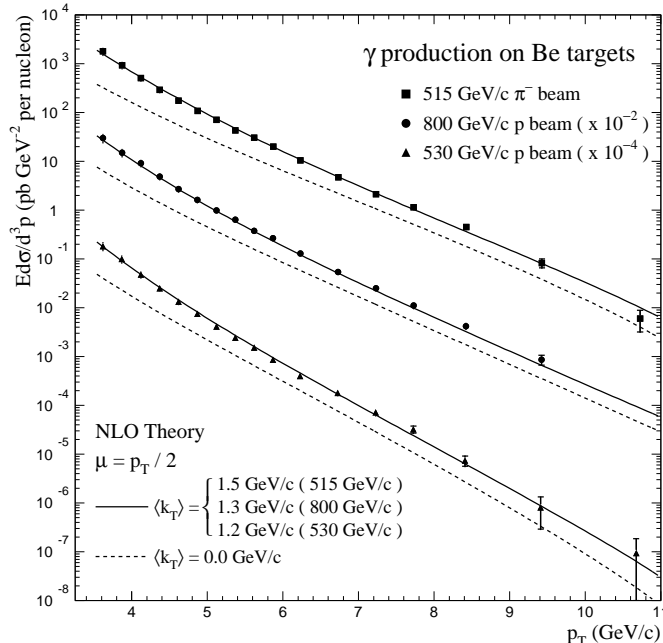


FIG. 28: Invariant differential cross sections per nucleon for direct-photon production as functions of  $p_T$ , averaged over rapidity, for 515 GeV/c  $\pi^-$  and 800 and 530 GeV/c proton beams incident upon beryllium. The error bars represent the statistical and systematic uncertainties combined in quadrature; the innermost interval indicates the statistical uncertainties. Overlaid on the data are NLO PQCD and  $k_T$ -enhanced NLO PQCD calculations. GRV92 PDF were used in the incident  $\pi^-$  calculations, while CTEQ5M PDF were used in the incident proton calculations.

beam particle types are different in the numerator and the denominator, the LO and NLO calculations are very different, and only the NLO result is consistent with our data for the PDF employed in these calculations.

Our direct-photon cross-section measurements, as illustrated in Figs. 24 and 25, as well as our  $\pi^0$  cross-section measurements reported in previous publications [9–11], are not satisfactorily described by the available NLO PQCD calculations. Similar discrepancies have been observed between PQCD calculations and other measurements of high- $p_T$  direct-photon and  $\pi^0$  production [48–50] and are attributed to the effect of initial-state soft-gluon radiation (see also Refs. [51–53]). The importance of including gluon emission through the resummation formalism has long been recognized, and the corresponding calculations have been available for some time for the diphoton process [54, 55]. However, these calculations have only recently been considered for inclusive direct-photon production [56–59]. While these developments are encouraging (e.g., see Fig. 2 of Ref. [58]), the calculations are still incomplete. In the absence of a rigorous treatment, the phenomenological prescription described in Refs. [9, 48] is used in the following comparisons of PQCD with our data. In this approach, soft-gluon radiation is parameterized in terms of an effective  $\langle k_T \rangle$  that provides an additional transverse impulse to the incoming partons. Since the hard-scattering cross sections fall steeply as functions of  $p_T$ , the net effect of this additional transverse impulse is to enhance high- $p_T$  yields. The  $k_T$  enhancement factors (as functions of  $p_T$ ) are evaluated by computing ratios of results from LO PQCD calculations [3] with and without  $k_T$ . These  $k_T$  enhancement factors are applied to the results of the NLO PQCD calculations. The  $\langle k_T \rangle$  values used in generating the  $k_T$  enhancement factors are representative of values that describe kinematic distributions observed in production of high-mass  $\pi^0\pi^0$ ,  $\gamma\pi^0$ , and  $\gamma\gamma$  systems [9, 34]. The  $k_T$ -enhanced NLO calculations are compared to our direct-photon measurements in Fig. 28, and provide a much improved description of our data (relative to the NLO calculations). Comparisons of the  $k_T$ -enhanced NLO calculations to our data as functions of  $y_{cm}$  for several  $p_T$  intervals are shown in Fig. 29 for 530 GeV/c  $p$  beam on beryllium.

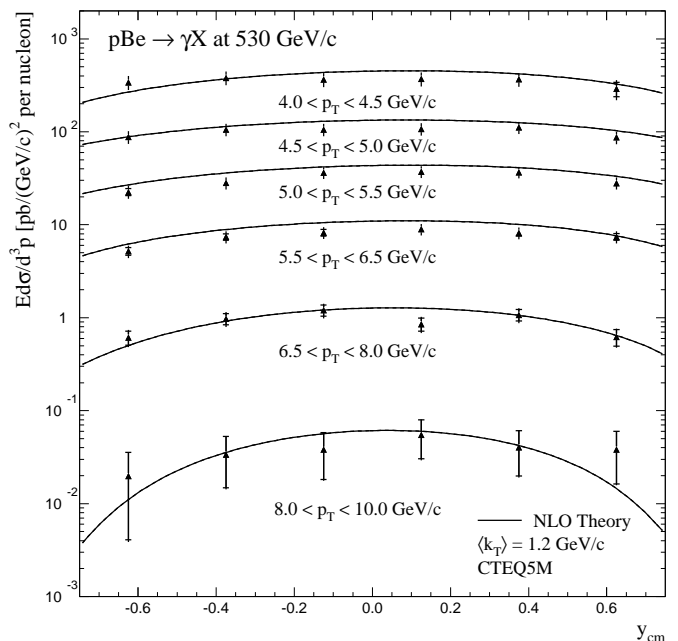


FIG. 29: Invariant differential cross sections per nucleon for direct-photon production as functions of  $y_{cm}$  in  $pBe$  interactions at 530 GeV/c for several intervals in  $p_T$ . The error bars represent the statistical and systematic uncertainties combined in quadrature; the innermost interval indicates the statistical uncertainties. Overlaid on the data are  $k_T$ -enhanced NLO PQCD calculations using the CTEQ5M PDF.

Results of  $k_T$  enhanced NLO PQCD calculations using CTEQ6.1M PDF [60, 61] are compared to our direct-photon measurements for incident protons in Fig. 30. The CTEQ6.1 PDF uncertainty bands are also shown in that figure. While the uncertainties associated with the PDF are small at low  $x_T$ , they are significantly larger than the uncertainties in data at moderate and high  $x_T$ , and are dominated by the uncertainty in the gluon distribution. There is also a large variation in the central value



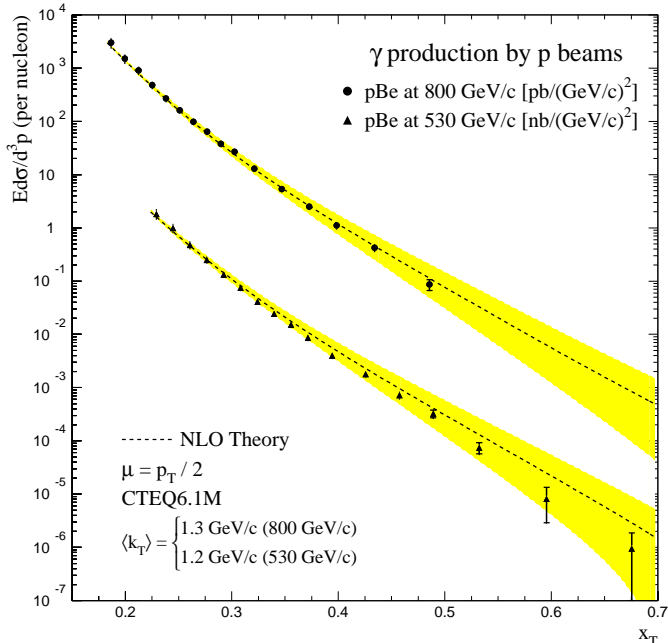


FIG. 30: Invariant differential cross sections per nucleon for direct-photon production as functions of  $x_T$  in  $p\text{Be}$  interactions at 800 and 530 GeV/c. The error bars represent the statistical and systematic uncertainties combined in quadrature; the innermost interval indicates the statistical uncertainties. Overlaid on the data are  $k_T$ -enhanced NLO PQCD calculations. The shaded region represents the uncertainty band associated with the CTEQ6.1M PDF set.

of several PDF sets, as illustrated in Fig. 31. The major difference between the CTEQ5M [62] and CTEQ6.1M PDF is that CTEQ6.1M has a much harder gluon (motivated by measurements of the inclusive jet cross section at the Tevatron collider). Cross sections calculated using MRST2003C PDF [63] are similar to results using CTEQ5M PDF. Figure 32 shows the ratio of the direct-photon cross sections from 800 GeV/c and 530 GeV/c  $p$  beams on beryllium, as a function of  $p_T$ , compared to results from  $k_T$ -enhanced NLO calculations using the MRST2003C, CTEQ5M, and CTEQ6.1M PDF. Calculations with PDF that have softer gluons provide a better description of our data at high  $p_T$ .

## V. CONCLUSIONS

High- $p_T$  direct-photon production has been measured in interactions of 515 GeV/c  $\pi^-$  and 530 GeV/c and 800 GeV/c protons with beryllium and hydrogen targets. The inclusive direct-photon cross sections were compared with NLO PQCD and  $k_T$ -enhanced NLO PQCD calculations for several choices of PDF. Without  $k_T$  enhancement, available NLO PQCD calculations do not satisfactorily represent our data. The data are described better by  $k_T$  enhanced NLO PQCD calculations using the softer gluons of CTEQ5 and MRST2003 than the harder gluons

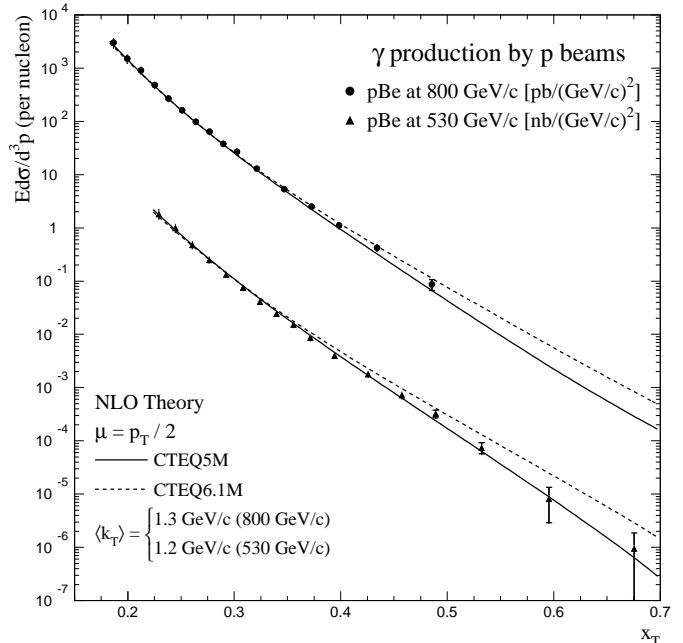


FIG. 31: Invariant differential cross sections per nucleon for direct-photon production as functions of  $x_T$  in  $p\text{Be}$  interactions at 800 and 530 GeV/c. The error bars represent the statistical and systematic uncertainties combined in quadrature; the innermost interval indicates the statistical uncertainties. Overlaid on the data are  $k_T$ -enhanced NLO PQCD calculations using CTEQ5M and CTEQ6.1M PDF.

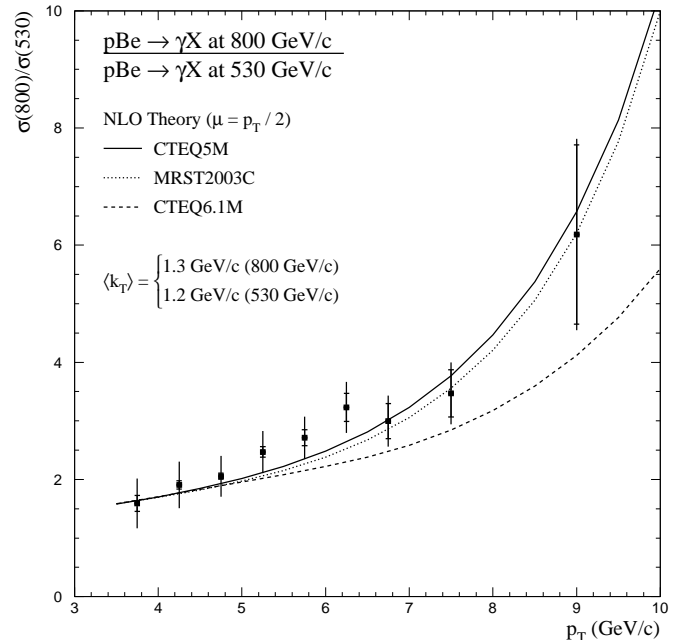


FIG. 32: The ratio of 800 to 530 GeV/c proton-beam direct-photon cross sections as a function of  $p_T$ . The error bars represent the statistical and systematic uncertainties combined in quadrature; the innermost interval indicates the statistical uncertainties. Results from  $k_T$ -enhanced NLO PQCD calculations are overlaid on the data.

of CTEQ6.1. As mentioned in the Introduction, direct-photon measurements provide potential constraints on the gluon, particularly at large  $x$ . This is especially relevant since recent global fits have used jet data from Tevatron Run I to constrain the large- $x$  gluon—thereby possibly incorporating new physics effects into the PDF [61]. We note that recent studies have suggested potential incompatibilities between the small- $x$  gluon determined using HERA data and the large- $x$  gluon required to fit the Tevatron jet data [64]. Inclusion of direct-photon data in the global fits would provide additional constraints on the gluon distribution, independent of the jet data from the Tevatron, thereby enhancing the discovery potential of the jet data being acquired in Tevatron Run II.

### Acknowledgments

We thank the U. S. Department of Energy, the National Science Foundation, including its Office of International Programs, and the Universities Grants Commission of India, for their support of this research. The staff and management of Fermilab are thanked for their efforts in making available the beam and computing facilities that made this work possible. We are pleased to acknowl-

edge the contributions of our colleagues on Fermilab experiment E672. We acknowledge the contributions of the following colleagues for their help in the operation and upgrade of the Meson West spectrometer: W. Dickerson and E. Pothier from Northeastern University; J. T. Anderson, E. Barsotti Jr., H. Koecher, P. Madsen, D. Petravick, R. Tokarek, J. Tweed, D. Allspach, J. Urbin, and the cryo crews from Fermi National Accelerator Laboratory; T. Haelen, C. Benson, L. Kuntz, and D. Ruggiero from the University of Rochester; the technical staffs of Michigan State University and Pennsylvania State University for the construction of the straw tubes and of the University of Pittsburgh for the silicon detectors. We thank the following commissioning run collaborators for their invaluable contributions to the hardware and software infrastructure of the original Meson West spectrometer: G. Alverson, G. Balloccchi, R. Benson, D. Berg, D. Brown, D. Carey, T. Chand, C. Chandlee, S. Easo, W. Faissler, G. Glass, I. Kourbanis, A. Lanaro, C. Nelson Jr., D. Orris, B. Rajaram, K. Ruddick, A. Sinanidis, and G. Wu. We also thank S. Catani, J.Ph. Guillet, B. Kniehl, J. Owens, G. Sterman, W. Vogelsang, and X.-N. Wang for many helpful discussions and for providing us with their QCD calculations.

- 
- [1] W. M. Geist et al., Phys. Rept. **197**, 263 (1990).  
 [2] N. A. McCubbin, Rep. Prog. Phys. **44**, 65 (1981).  
 [3] J. F. Owens, Rev. Mod. Phys. **59**, 465 (1987).  
 [4] T. Ferbel and W. R. Molzon, Rev. Mod. Phys. **56**, 181 (1984).  
 [5] J. Huston et al., Phys. Rev. **D58**, 114034 (1998).  
 [6] H. L. Lai et al., Phys. Rev. **D55**, 1280 (1997).  
 [7] M. Gluck, E. Reya, and A. Vogt, Z. Phys. **C53**, 127 (1992).  
 [8] A. D. Martin, R. G. Roberts, W. J. Stirling, and R. S. Thorne, Eur. Phys. J. **C4**, 463 (1998).  
 [9] L. Apanasevich et al., Phys. Rev. Lett. **81**, 2642 (1998).  
 [10] L. Apanasevich et al., Phys. Rev. **D68**, 052001 (2003). A computational error in the correction of measured cross sections for contributions from minority particles in secondary beams affected the reported cross sections for  $\pi^0$  and  $\eta$  production by 530 GeV/ $c$  protons. As a result, the cross sections listed in the tables for 530 GeV/ $c$  protons in the publication referenced here should be increased by 3.4%, a change that falls well within the quoted systematic uncertainties.  
 [11] L. Apanasevich et al., Phys. Rev. **D69**, 032003 (2004).  
 [12] L. Apanasevich et al., Phys. Rev. **D56**, 1391 (1997).  
 [13] L. Apanasevich et al. (2000), hep-ex/0004012.  
 [14] G. Alverson et al., Phys. Rev. **D48**, 5 (1993).  
 [15] G. Alverson et al., Phys. Rev. **D49**, 3106 (1994).  
 [16] The event samples presented in this paper exclude data collected during the 1987-1988 commissioning run of E706 (presented in Ref. [14] and references therein). Although our earlier data are generally consistent with the results reported here, once systematic differences between the two analyses are properly accounted for, the results from the initial run are superseded by our current higher statistics, more precise data samples. Theoretical calculations presented here also supersede earlier calculations.  
 [17] D. Allspach et al., Adv. Cryog. Eng. **37**, 1495 (1991).  
 [18] C. Bromberg et al., Nucl. Inst. & Meth. **A307**, 292 (1991).  
 [19] L. Apanasevich et al., Nucl. Inst. & Meth. **A417**, 50 (1998).  
 [20] A. Gribushin et al., Phys. Rev. **D53**, 4723 (1996).  
 [21] A. Gribushin et al., Phys. Rev. **D62**, 012001 (2000).  
 [22] V. Koreshev et al., Phys. Rev. Lett. **77**, 4294 (1996).  
 [23] R. Jesik et al., Phys. Rev. Lett. **74**, 495 (1995).  
 [24] D. Striley, Ph.D. thesis, University of Missouri-Columbia (1996).  
 [25] L. Sorrell, *The E706 Trigger System*, E706 Note 201, 1994 (unpublished); Ph.D. thesis, Michigan State University, 1995; G. Osborne, Ph.D. thesis, University of Rochester, 1996.  
 [26] During the 1990 run, the beam hole definition was implemented using a single scintillation counter. An array of four scintillation counters was used for the beam hole definition during the 1991-1992 run.  
 [27] G. Corcella et al., JHEP, **01**, (2001) 010, HERWIG v6.1. HERWIG v6.1 was used as the event generator for the vertex efficiency studies. The relative normalizations of the simulated samples from various targets were tuned to match the data.  
 [28] F. Carminati et al., GEANT: Detector Description and Simulation Tool, CERN Program Library Long Writeup W5013, 1993.  
 [29] G. Marchesini et al., Comput. Phys. Commun. **67**, 465

- (1992), HERWIG v5.6.
- [30] L. Apanasevich, Ph.D. thesis, Michigan State University (in preparation).
- [31] Our measured  $\eta/\pi^0$  ratios as functions of  $p_T$  were fit to constants for  $p_T > 3.0$  GeV/ $c$ . For the 515 GeV/ $c$   $\pi^-$ Be interactions, the resulting  $\eta/\pi^0$  is  $0.48 \pm 0.01(\text{stat})$ . The relevant data is shown in Fig. 15 of Ref. [11]. The corresponding  $\eta/\pi^0$  from the 800 GeV/ $c$   $p$ Be interactions is  $0.42 \pm 0.01(\text{stat})$ , while for the 530 GeV/ $c$   $p$ Be interactions the result is  $0.45 \pm 0.01(\text{stat})$  [10]. The generated  $\eta$  spectra were weighted to match the shape of our measured  $\pi^0$  spectra, invoking appropriate relative normalization factors.
- [32] As illustrated in Fig. 10.1 of Ref [65], HERWIG v5.6 provides a good description of the  $\omega$  to  $\pi^0$  ratio observed in our data. However, Ref. [13] shows that HERWIG v6.1 generates a much smaller  $\omega$  to  $\pi^0$  production ratio. HERWIG v5.6 was used to generate the DGS samples employed in the evaluation of the direct-photon backgrounds.
- [33] The  $\eta'/\pi^0$  ratio from HERWIG v5.6 is  $\approx 0.2$ . A measurement of this high- $p_T$  production ratio yields  $0.85 \pm 0.24$  (after updating the  $\eta' \rightarrow \gamma\gamma$  branching ratio) [35, 36]. This difference has been included as a contribution to the systematic uncertainties in the direct-photon background.
- [34] M. Begel, Ph.D. thesis, University of Rochester (1999).
- [35] M. Diakonou et al., Phys. Lett. **89B**, 432 (1980).
- [36] D. E. Groom et al., Eur. Phys. J. **C15**, 1 (2000).
- [37] P. Aurenche et al., Phys. Lett. **B140**, 87 (1984).
- [38] E. L. Berger and J. Qiu, Phys. Rev. **D44**, 2002 (1991).
- [39] G. D. Lafferty and T. R. Wyatt, Nucl. Instrum. Methods Phys. Res. **A355**, 541 (1995).
- [40] Xin-Nian Wang, Nucl. Phys. **A661**, 609 (1999), and private communication with Xin-Nian Wang regarding the use of this program at our beam energies.
- [41] E. Laenen, G. Oderda, and G. Sterman, Phys. Lett. **B438**, 173 (1998).
- [42] S. Catani et al., JHEP **03**, 025 (1999).
- [43] N. Kidonakis and J. F. Owens, Phys. Rev. **D61**, 094004 (2000).
- [44] G. Sterman and W. Vogelsang, JHEP **02**, 016 (2001).
- [45] N. Kidonakis and J. F. Owens (2003), hep-ph/0307352.
- [46] A. D. Martin, R. G. Roberts, W. J. Stirling, and R. S. Thorne, Eur. Phys. J. **C23**, 73 (2002).
- [47] A. D. Martin, R. G. Roberts, W. J. Stirling, and R. S. Thorne, Eur. Phys. J. **C28**, 455 (2003).
- [48] L. Apanasevich et al., Phys. Rev. **D59**, 074007 (1999).
- [49] L. Apanasevich et al., Phys. Rev. **D63**, 014009 (2001).
- [50] S. Chekanov et al., Phys. Lett. **511B**, 19 (2001).
- [51] J. Huston et al., Phys. Rev. **D51**, 6139 (1995).
- [52] P. Aurenche et al., Eur. Phys. J. **C9**, 107 (1999).
- [53] P. Aurenche et al., Eur. Phys. J. **C13**, 347 (2000).
- [54] C. Balázs et al., Phys. Rev. **D57**, 6934 (1998).
- [55] P. Chiappetta, R. Fergani, and J. Guillet, Phys. Lett. **B348**, 646 (1995).
- [56] H.-L. Lai and H. Li, Phys. Rev. **D58**, 114020 (1998).
- [57] H. Li, Phys. Lett. **B454**, 328 (1999).
- [58] E. Laenen, G. Sterman, and W. Vogelsang, Phys. Rev. Lett. **84**, 4296 (2000).
- [59] E. Laenen, G. Sterman, and W. Vogelsang, Phys. Rev. **D63**, 114018 (2001).
- [60] J. Pumplin et al., JHEP **07**, 012 (2002).
- [61] D. Stump et al., JHEP **10**, 046 (2003).
- [62] H. L. Lai et al., Eur. Phys. J. **C12**, 375 (2000).
- [63] A. D. Martin, R. G. Roberts, W. J. Stirling, and R. S. Thorne (2003), hep-ph/0307262.
- [64] A. D. Martin, R. G. Roberts, W. J. Stirling, and R. S. Thorne, (2003), hep-ph/0308087; J. Stirling, presentation at the Collider Physics conference, Kavli Institute for Theoretical Physics, Santa Barbara, January 2004.
- [65] L. de Barbaro, Ph.D. thesis, University of Rochester (1995).

## APPENDIX: TABULATED CROSS SECTIONS

TABLE I: Invariant differential cross sections ( $E d\sigma/d^3p$ ) per nucleon for direct-photon production in  $p\text{Be}$  collisions at 800 and 530 GeV/ $c$ , and  $\pi^- \text{Be}$  collisions at 515 GeV/ $c$  as functions of  $p_T$ .

$p_T$ (GeV/ $c$ )	$p\text{Be}$ at 800 GeV/ $c$	$p\text{Be}$ at 530 GeV/ $c$	$\pi^- \text{Be}$ at 515 GeV/ $c$
	$-1.0 \leq y_{\text{cm}} \leq 0.5$ [nb/(GeV/ $c$ ) <sup>2</sup> ]	$-0.75 \leq y_{\text{cm}} \leq 0.75$ [nb/(GeV/ $c$ ) <sup>2</sup> ]	$-0.75 \leq y_{\text{cm}} \leq 0.75$ [nb/(GeV/ $c$ ) <sup>2</sup> ]
3.50 – 3.75	$2.99 \pm 0.24 \pm 0.62$	$1.83 \pm 0.17 \pm 0.37$	$1.79 \pm 0.10 \pm 0.33$
3.75 – 4.00	$1.500 \pm 0.091 \pm 0.29$	$0.993 \pm 0.062 \pm 0.18$	$0.924 \pm 0.036 \pm 0.16$
4.00 – 4.25	$0.908 \pm 0.031 \pm 0.16$	$0.478 \pm 0.019 \pm 0.081$	$0.5058 \pm 0.0081 \pm 0.080$
4.25 – 4.50	$0.482 \pm 0.011 \pm 0.079$	$0.2508 \pm 0.0047 \pm 0.040$	$0.2891 \pm 0.0052 \pm 0.043$
4.50 – 4.75	$0.2679 \pm 0.0068 \pm 0.041$	$0.1334 \pm 0.0030 \pm 0.020$	$0.1736 \pm 0.0034 \pm 0.024$
4.75 – 5.00	$0.1616 \pm 0.0042 \pm 0.023$	$0.0757 \pm 0.0021 \pm 0.011$	$0.1084 \pm 0.0024 \pm 0.014$
	[pb/(GeV/ $c$ ) <sup>2</sup> ]	[pb/(GeV/ $c$ ) <sup>2</sup> ]	[pb/(GeV/ $c$ ) <sup>2</sup> ]
5.00 – 5.25	$98.4 \pm 3.1 \pm 14$	$41.3 \pm 1.4 \pm 5.5$	$70.8 \pm 1.8 \pm 9.0$
5.25 – 5.50	$63.7 \pm 2.3 \pm 8.4$	$24.4 \pm 1.0 \pm 3.2$	$42.7 \pm 1.3 \pm 5.2$
5.50 – 5.75	$37.7 \pm 1.6 \pm 4.8$	$15.16 \pm 0.74 \pm 1.9$	$30.6 \pm 1.0 \pm 3.7$
5.75 – 6.00	$26.7 \pm 1.3 \pm 3.3$	$8.60 \pm 0.55 \pm 1.1$	$20.02 \pm 0.77 \pm 2.4$
6.00 – 6.50	$12.86 \pm 0.52 \pm 1.6$	$3.98 \pm 0.25 \pm 0.49$	$10.38 \pm 0.37 \pm 1.2$
6.50 – 7.00	$5.36 \pm 0.30 \pm 0.63$	$1.79 \pm 0.15 \pm 0.22$	$4.74 \pm 0.23 \pm 0.55$
7.00 – 7.50	$2.51 \pm 0.19 \pm 0.29$	$0.718 \pm 0.086 \pm 0.089$	$2.12 \pm 0.15 \pm 0.25$
7.50 – 8.00	$1.11 \pm 0.12 \pm 0.13$	$0.324 \pm 0.054 \pm 0.041$	$1.148 \pm 0.099 \pm 0.14$
8.00 – 9.00	$0.420 \pm 0.052 \pm 0.049$	$0.074 \pm 0.018 \pm 0.010$	$0.452 \pm 0.041 \pm 0.054$
9.00 – 10.00	$0.086 \pm 0.020 \pm 0.010$	$0.0082 \pm 0.0053 \pm 0.0012$	$0.083 \pm 0.017 \pm 0.010$
10.00 – 12.00		$0.00095 \pm 0.00095 \pm 0.00015$	$0.0060 \pm 0.0028 \pm 0.0008$

TABLE II: Invariant differential cross sections ( $E d\sigma/d^3p$ ) for direct-photon production in  $pp$  collisions at 800 and 530 GeV/ $c$ , and  $\pi^- p$  collisions at 515 GeV/ $c$  as functions of  $p_T$ .

$p_T$ (GeV/ $c$ )	$pp$ at 800 GeV/ $c$	$pp$ at 530 GeV/ $c$	$\pi^- p$ at 515 GeV/ $c$
	$-1.0 \leq y_{\text{cm}} \leq 0.5$ [nb/(GeV/ $c$ ) <sup>2</sup> ]	$-0.75 \leq y_{\text{cm}} \leq 0.75$ [nb/(GeV/ $c$ ) <sup>2</sup> ]	$-0.75 \leq y_{\text{cm}} \leq 0.75$ [nb/(GeV/ $c$ ) <sup>2</sup> ]
3.50 – 4.00	$1.88 \pm 0.30 \pm 0.38$	$1.16 \pm 0.19 \pm 0.22$	$1.72 \pm 0.42 \pm 0.31$
4.00 – 4.50	$0.600 \pm 0.044 \pm 0.10$	$0.375 \pm 0.030 \pm 0.062$	$0.493 \pm 0.028 \pm 0.076$
4.50 – 5.00	$0.2255 \pm 0.0094 \pm 0.034$	$0.1076 \pm 0.0045 \pm 0.016$	$0.165 \pm 0.011 \pm 0.022$
	[pb/(GeV/ $c$ ) <sup>2</sup> ]	[pb/(GeV/ $c$ ) <sup>2</sup> ]	[pb/(GeV/ $c$ ) <sup>2</sup> ]
5.00 – 5.50	$82.2 \pm 4.4 \pm 11$	$33.6 \pm 2.2 \pm 4.4$	$64.8 \pm 6.0 \pm 8.1$
5.50 – 6.00	$35.0 \pm 2.4 \pm 4.4$	$11.4 \pm 1.1 \pm 1.4$	$25.5 \pm 3.5 \pm 3.0$
6.00 – 7.00	$9.80 \pm 0.74 \pm 1.2$	$3.43 \pm 0.37 \pm 0.42$	$9.0 \pm 1.3 \pm 1.0$
7.00 – 8.00	$1.73 \pm 0.28 \pm 0.20$	$0.42 \pm 0.11 \pm 0.05$	$2.81 \pm 0.62 \pm 0.33$
8.00 – 10.00	$0.339 \pm 0.070 \pm 0.039$	$0.010 \pm 0.015 \pm 0.001$	$0.30 \pm 0.14 \pm 0.04$
10.00 – 12.00	$0.017 \pm 0.014 \pm 0.002$		

TABLE III: The invariant differential cross section ( $Ed\sigma/d^3p$ ) per nucleon as a function of  $y_{\text{cm}}$  and  $p_T$  for the inclusive reaction  $p\text{Be} \rightarrow \gamma X$  at 530 GeV/c.

$p_T$ (GeV/c)	$-0.75 \leq y_{\text{cm}} \leq -0.50$ [pb/(GeV/c) <sup>2</sup> ]	$-0.50 \leq y_{\text{cm}} \leq -0.25$ [pb/(GeV/c) <sup>2</sup> ]	$-0.25 \leq y_{\text{cm}} \leq 0.00$ [pb/(GeV/c) <sup>2</sup> ]
3.50 - 4.00	1150 ± 220 ± 210	1470 ± 210 ± 270	1390 ± 220 ± 260
4.00 - 4.50	339 ± 14 ± 57	381 ± 12 ± 64	365 ± 11 ± 62
4.50 - 5.00	87.9 ± 4.3 ± 13	105.5 ± 4.5 ± 16	105.4 ± 4.7 ± 16
5.00 - 5.50	22.5 ± 1.9 ± 3.0	28.2 ± 2.0 ± 3.8	36.4 ± 2.3 ± 4.9
5.50 - 6.50	5.19 ± 0.48 ± 0.65	7.41 ± 0.60 ± 0.92	8.25 ± 0.68 ± 1.0
6.50 - 8.00	0.61 ± 0.11 ± 0.08	0.97 ± 0.14 ± 0.12	1.20 ± 0.16 ± 0.15
8.00 - 10.00	0.020 ± 0.016 ± 0.003	0.034 ± 0.019 ± 0.005	0.038 ± 0.020 ± 0.005
	$0.00 \leq y_{\text{cm}} \leq 0.25$	$0.25 \leq y_{\text{cm}} \leq 0.50$	$0.50 \leq y_{\text{cm}} \leq 0.75$
3.50 - 4.00	1510 ± 190 ± 280	1570 ± 160 ± 290	1120 ± 260 ± 200
4.00 - 4.50	370.8 ± 9.9 ± 63	367.2 ± 9.3 ± 62	290 ± 52 ± 49
4.50 - 5.00	107.2 ± 4.3 ± 16	111.4 ± 4.2 ± 16	87.1 ± 4.0 ± 13
5.00 - 5.50	37.2 ± 2.2 ± 5.0	36.8 ± 2.1 ± 4.9	28.1 ± 2.0 ± 3.8
5.50 - 6.50	8.95 ± 0.65 ± 1.1	8.19 ± 0.63 ± 1.0	7.42 ± 0.61 ± 0.92
6.50 - 8.00	0.85 ± 0.14 ± 0.11	1.07 ± 0.15 ± 0.13	0.62 ± 0.13 ± 0.08
8.00 - 10.00	0.055 ± 0.025 ± 0.007	0.040 ± 0.021 ± 0.005	0.038 ± 0.022 ± 0.005

TABLE IV: The invariant differential cross section ( $Ed\sigma/d^3p$ ) per nucleon as a function of  $y_{\text{cm}}$  and  $p_T$  for the inclusive reaction  $p\text{Be} \rightarrow \gamma X$  at 800 GeV/c.

$p_T$ (GeV/c)	$-1.0 \leq y_{\text{cm}} \leq -0.75$ [pb/(GeV/c) <sup>2</sup> ]	$-0.75 \leq y_{\text{cm}} \leq -0.50$ [pb/(GeV/c) <sup>2</sup> ]	$-0.50 \leq y_{\text{cm}} \leq -0.25$ [pb/(GeV/c) <sup>2</sup> ]
3.50 - 4.00	1200 ± 320 ± 230	2000 ± 320 ± 380	2020 ± 320 ± 380
4.00 - 4.50	516 ± 43 ± 90	499 ± 44 ± 87	703 ± 44 ± 120
4.50 - 5.00	129.3 ± 7.4 ± 20	157.7 ± 8.2 ± 24	218.8 ± 8.9 ± 33
5.00 - 5.50	44.2 ± 3.8 ± 6.0	64.6 ± 4.0 ± 8.8	78.2 ± 4.6 ± 11
5.50 - 6.50	10.31 ± 0.93 ± 1.3	18.5 ± 1.3 ± 2.3	23.3 ± 1.4 ± 2.9
6.50 - 8.00	1.35 ± 0.18 ± 0.16	1.93 ± 0.24 ± 0.23	3.41 ± 0.32 ± 0.40
8.00 - 10.00	0.170 ± 0.045 ± 0.020	0.169 ± 0.046 ± 0.020	0.325 ± 0.070 ± 0.038
	$-0.25 \leq y_{\text{cm}} \leq 0.00$	$0.00 \leq y_{\text{cm}} \leq 0.25$	$0.25 \leq y_{\text{cm}} \leq 0.50$
3.50 - 4.00	3710 ± 410 ± 700	2680 ± 250 ± 510	1870 ± 250 ± 350
4.00 - 4.50	792 ± 39 ± 140	898 ± 38 ± 160	763 ± 35 ± 130
4.50 - 5.00	234.7 ± 8.5 ± 36	297 ± 12 ± 45	250 ± 12 ± 38
5.00 - 5.50	95.5 ± 4.6 ± 13	100.5 ± 5.5 ± 14	103.4 ± 5.6 ± 14
5.50 - 6.50	27.2 ± 1.4 ± 3.4	30.7 ± 1.6 ± 3.8	25.1 ± 1.6 ± 3.1
6.50 - 8.00	3.78 ± 0.32 ± 0.44	4.19 ± 0.37 ± 0.49	3.29 ± 0.37 ± 0.38
8.00 - 10.00	0.149 ± 0.054 ± 0.017	0.285 ± 0.076 ± 0.033	0.412 ± 0.100 ± 0.048

TABLE V: The invariant differential cross section ( $E d\sigma/d^3p$ ) per nucleon as a function of  $y_{\text{cm}}$  and  $p_T$  for the inclusive reaction  $\pi^- \text{Be} \rightarrow \gamma X$  at 515 GeV/c.

$p_T$ (GeV/c)	$-0.75 \leq y_{\text{cm}} \leq -0.50$ [pb/(GeV/c) <sup>2</sup> ]	$-0.50 \leq y_{\text{cm}} \leq -0.25$ [pb/(GeV/c) <sup>2</sup> ]	$-0.25 \leq y_{\text{cm}} \leq 0.00$ [pb/(GeV/c) <sup>2</sup> ]
3.50 – 4.00	1250 ± 220 ± 210	1150 ± 100 ± 190	1312 ± 88 ± 220
4.00 – 4.50	370 ± 15 ± 58	342 ± 11 ± 53	401 ± 11 ± 63
4.50 – 5.00	80.4 ± 5.0 ± 11	124.3 ± 4.7 ± 17	137.4 ± 5.1 ± 19
5.00 – 5.50	30.7 ± 2.2 ± 3.9	48.0 ± 2.5 ± 6.0	54.6 ± 2.7 ± 6.8
5.50 – 6.50	8.63 ± 0.64 ± 1.0	12.79 ± 0.79 ± 1.5	18.51 ± 0.93 ± 2.2
6.50 – 8.00	0.96 ± 0.14 ± 0.11	1.76 ± 0.19 ± 0.20	2.84 ± 0.24 ± 0.33
8.00 – 10.00	0.060 ± 0.029 ± 0.007	0.159 ± 0.040 ± 0.019	0.294 ± 0.056 ± 0.035
	$0.00 \leq y_{\text{cm}} \leq 0.25$	$0.25 \leq y_{\text{cm}} \leq 0.50$	$0.50 \leq y_{\text{cm}} \leq 0.75$
3.50 – 4.00	1670 ± 120 ± 280	1490 ± 100 ± 250	1240 ± 67 ± 210
4.00 – 4.50	436 ± 11 ± 68	444 ± 11 ± 69	387 ± 11 ± 61
4.50 – 5.00	162.7 ± 5.1 ± 22	175.2 ± 5.4 ± 24	165.5 ± 5.4 ± 23
5.00 – 5.50	64.1 ± 2.7 ± 8.1	73.2 ± 2.9 ± 9.2	69.1 ± 3.0 ± 8.7
5.50 – 6.50	21.73 ± 0.95 ± 2.6	23.30 ± 0.99 ± 2.8	21.9 ± 1.0 ± 2.6
6.50 – 8.00	3.22 ± 0.25 ± 0.37	4.09 ± 0.29 ± 0.47	3.10 ± 0.28 ± 0.36
8.00 – 10.00	0.424 ± 0.065 ± 0.051	0.367 ± 0.068 ± 0.044	0.237 ± 0.053 ± 0.028

TABLE VI: The invariant differential cross section ( $E d\sigma/d^3p$ ) as a function of  $y_{\text{cm}}$  and  $p_T$  for the inclusive reaction  $pp \rightarrow \gamma X$  at 530 GeV/c.

$p_T$ (GeV/c)	$-0.75 \leq y_{\text{cm}} \leq -0.50$ [pb/(GeV/c) <sup>2</sup> ]	$-0.50 \leq y_{\text{cm}} \leq -0.25$ [pb/(GeV/c) <sup>2</sup> ]	$-0.25 \leq y_{\text{cm}} \leq 0.00$ [pb/(GeV/c) <sup>2</sup> ]
3.50 – 4.00	2210 ± 570 ± 400	1180 ± 480 ± 220	850 ± 420 ± 160
4.00 – 4.50	356 ± 32 ± 60	363 ± 28 ± 61	411 ± 25 ± 69
4.50 – 5.00	93 ± 12 ± 14	112 ± 11 ± 16	128 ± 11 ± 19
5.00 – 5.50	24.8 ± 5.1 ± 3.3	35.8 ± 5.0 ± 4.8	38.0 ± 5.6 ± 5.1
5.50 – 6.50	5.6 ± 1.2 ± 0.7	9.3 ± 1.6 ± 1.2	6.9 ± 1.6 ± 0.9
6.50 – 8.00	0.25 ± 0.20 ± 0.03	0.84 ± 0.32 ± 0.10	0.87 ± 0.34 ± 0.11
	$0.00 \leq y_{\text{cm}} \leq 0.25$	$0.25 \leq y_{\text{cm}} \leq 0.50$	$0.50 \leq y_{\text{cm}} \leq 0.75$
3.50 – 4.00	1110 ± 390 ± 200	800 ± 240 ± 150	560 ± 520 ± 100
4.00 – 4.50	315 ± 23 ± 53	327 ± 22 ± 55	390 ± 160 ± 70
4.50 – 5.00	110 ± 11 ± 16	103.7 ± 9.6 ± 15	72.9 ± 9.2 ± 11
5.00 – 5.50	36.0 ± 5.3 ± 4.8	33.0 ± 5.1 ± 4.4	24.2 ± 4.7 ± 3.2
5.50 – 6.50	10.4 ± 1.7 ± 1.3	10.0 ± 1.6 ± 1.2	4.0 ± 1.3 ± 0.5
6.50 – 8.00	1.01 ± 0.35 ± 0.12	1.65 ± 0.41 ± 0.20	0.60 ± 0.27 ± 0.07

TABLE VII: The invariant differential cross section ( $E d\sigma/d^3p$ ) as a function of  $y_{\text{cm}}$  and  $p_T$  for the inclusive reaction  $pp \rightarrow \gamma X$  at 800 GeV/ $c$ .

$p_T$ (GeV/ $c$ )	$-1.0 \leq y_{\text{cm}} \leq -0.75$ [pb/(GeV/ $c$ ) <sup>2</sup> ]	$-0.75 \leq y_{\text{cm}} \leq -0.50$ [pb/(GeV/ $c$ ) <sup>2</sup> ]	$-0.50 \leq y_{\text{cm}} \leq -0.25$ [pb/(GeV/ $c$ ) <sup>2</sup> ]
3.50 - 4.00	1990 ± 870 ± 380	1320 ± 790 ± 250	990 ± 780 ± 190
4.00 - 4.50	483 ± 72 ± 84		744 ± 83 ± 130
4.50 - 5.00	162 ± 20 ± 25	211 ± 20 ± 32	219 ± 21 ± 33
5.00 - 5.50	44.0 ± 7.6 ± 6.0	78.9 ± 9.6 ± 11	84 ± 11 ± 11
5.50 - 6.50	12.6 ± 2.3 ± 1.6	20.8 ± 3.0 ± 2.6	25.0 ± 3.3 ± 3.1
6.50 - 8.00	1.69 ± 0.49 ± 0.20	2.20 ± 0.64 ± 0.26	3.02 ± 0.79 ± 0.35
8.00 - 10.00	0.18 ± 0.11 ± 0.02	0.45 ± 0.20 ± 0.05	0.44 ± 0.19 ± 0.05
	$-0.25 \leq y_{\text{cm}} \leq 0.00$	$0.00 \leq y_{\text{cm}} \leq 0.25$	$0.25 \leq y_{\text{cm}} \leq 0.50$
3.50 - 4.00	2290 ± 810 ± 430	2510 ± 570 ± 470	2190 ± 550 ± 410
4.00 - 4.50	801 ± 52 ± 140	810 ± 100 ± 140	621 ± 79 ± 110
4.50 - 5.00	208 ± 19 ± 31	330 ± 27 ± 50	222 ± 30 ± 34
5.00 - 5.50	85 ± 10 ± 12	111 ± 13 ± 15	90 ± 13 ± 12
5.50 - 6.50	30.4 ± 3.5 ± 3.8	31.5 ± 3.8 ± 3.9	23.7 ± 3.8 ± 2.9
6.50 - 8.00	3.74 ± 0.79 ± 0.44	5.28 ± 0.96 ± 0.62	4.18 ± 0.94 ± 0.49
8.00 - 10.00	0.25 ± 0.16 ± 0.03		0.77 ± 0.23 ± 0.09

TABLE VIII: The invariant differential cross section ( $E d\sigma/d^3p$ ) as a function of  $y_{\text{cm}}$  and  $p_T$  for the inclusive reaction  $\pi^- p \rightarrow \gamma X$  at 515 GeV/ $c$ .

$p_T$ (GeV/ $c$ )	$-0.75 \leq y_{\text{cm}} \leq -0.50$ [pb/(GeV/ $c$ ) <sup>2</sup> ]	$-0.50 \leq y_{\text{cm}} \leq -0.25$ [pb/(GeV/ $c$ ) <sup>2</sup> ]	$-0.25 \leq y_{\text{cm}} \leq 0.00$ [pb/(GeV/ $c$ ) <sup>2</sup> ]
4.00 - 4.50	477 ± 76 ± 74	454 ± 79 ± 71	566 ± 71 ± 88
4.50 - 5.00	156 ± 26 ± 21	158 ± 27 ± 22	189 ± 29 ± 26
5.00 - 5.50	43 ± 12 ± 5.0	52 ± 14 ± 6.0	73 ± 16 ± 9.0
5.50 - 6.50	6.5 ± 3.5 ± 0.8	14.2 ± 4.6 ± 1.7	20.5 ± 5.0 ± 2.4
6.50 - 8.00	2.1 ± 1.0 ± 0.2	2.9 ± 1.2 ± 0.3	4.0 ± 1.5 ± 0.5
	$0.00 \leq y_{\text{cm}} \leq 0.25$	$0.25 \leq y_{\text{cm}} \leq 0.50$	$0.50 \leq y_{\text{cm}} \leq 0.75$
4.00 - 4.50	514 ± 64 ± 80	547 ± 57 ± 85	403 ± 66 ± 63
4.50 - 5.00	137 ± 26 ± 19	208 ± 29 ± 29	145 ± 29 ± 20
5.00 - 5.50	65 ± 14 ± 8.0	84 ± 16 ± 11	72 ± 16 ± 9.0
5.50 - 6.50	25.9 ± 5.3 ± 3.1	25.0 ± 5.5 ± 3.0	19.8 ± 5.5 ± 2.3
6.50 - 8.00	4.7 ± 1.6 ± 0.5	4.7 ± 1.6 ± 0.5	4.9 ± 1.9 ± 0.6